

Predicting Frictional Properties of Graphene Kirigami Using Molecular Dynamics and Neural Networks

Designs for a negative friction coefficient.

Mikkel Metzsch Jensen



Thesis submitted for the degree of
Master in Computational Science: Materials Science
60 credits

Department of Physics
Faculty of mathematics and natural sciences

UNIVERSITY OF OSLO

Spring 2023

Predicting Frictional Properties of Graphene Kirigami Using Molecular Dynamics and Neural Networks

Designs for a negative friction coefficient.

Mikkel Metzsch Jensen



© 2023 Mikkel Metzsch Jensen

Predicting Frictional Properties of Graphene Kirigami Using Molecular Dynamics and Neural Networks

<http://www.duo.uio.no/>

Printed: Reprocentralen, University of Oslo

Abstract

Abstract.

Acknowledgments

Acknowledgments.

List of Symbols

F_N Normal force (normal load)

Acronyms

AFM Atomic Force microscope. 21, 22, 23, 25

FFM Friction Force Microscopes. 21, 22, 23, 24, 25

FK Frenkel-Kontorova. 11, 16, 17, 18, 19, 20, 23, 24

FKT Frenkel–Kontorova–Tomlinson. 11, 20, 23, 24

GS Ground State. 17, 18

MD Molecular Dynamics. 1, 2, 3, 10, 11, 12, 14, 23, 24, 25, 26, 29, 33, 34, 35

ML Machine Learning. 2, 3, 35

PT Prandtl–Tomlinson. 11, 16, 17, 19, 20, 22, 23, 25

SFA Surface force apparatus. 22, 23

SFM Scanning Force Microscopies. 21

SPM Scanning Probe Microscopy. 21

Contents

1	Introduction	1
1.1	Motivation	1
1.2	Goals	2
1.3	Contributions	3
1.4	Thesis structure	3
I	Background Theory	5
2	Friction	7
2.1	Friction across scales	7
2.2	Macroscale	7
2.2.1	Amontons' law	7
2.3	Microscopic scale	9
2.3.1	Asperity theories	9
2.4	Nanoscale — Atomic scale	10
2.4.1	Prandtl–Tomlinson	11
2.4.1.1	Thermal activation	12
2.4.1.2	Sliding speed	14
2.4.1.3	Tip mass	15
2.4.1.4	Friction Regimes: Smooth Sliding, Single Slip, and Multiple Slip	15
2.4.2	Frenkel–Kontorova	16
2.4.2.1	Commensurability	17
2.4.2.2	Velocity resonance	19
2.4.3	Frenkel–Kontorova–Tomlinson	20
2.4.4	Shortcomings of atomic models	21
2.4.5	Experimental procedures	21
2.4.5.1	Scanning Probe Microscopy	21
2.4.5.2	Surface Force Apparatus	22
2.5	Summary of previous results	22
2.6	Research questions	25
II	Simulations	27
3	Negative friction coefficient	29
3.1	Nanomachine coupling	29
4	Summary	33
4.1	Summary and conclusions	33
4.1.1	Designing an MD simulation	33
4.1.2	Generetig Kirigami patterns	34
4.1.3	Control friction using Kirigami	34
4.1.4	Capture trends with machine learning	34

4.1.5 Accelerated search	35
4.1.6 Negative friction coefficient	36
4.2 Outlook	36
Appendices	37
A Appendix A	39
A Appendix B	41
B Appendix C	43

Chapter 1

Introduction

1.1 Motivation

Friction is the force that prevents the relative motion of objects in contact. Even though the everyday person might not be familiar with the term *friction* we recognize it as the inherent resistance to sliding motion. Some surfaces appear slippery and some rough, and we know intuitively that sliding down a snow-covered hill is much more exciting than its grassy counterpart. Without friction, it would not be possible to walk across a flat surface, lean against the wall without falling over or secure an object by the use of nails or screws [p. 5] [1]. It is probably safe to say that the concept of friction is integrated into our everyday life to such an extent that most people take it for granted. However, the efforts to control friction date back to the early civilization (3500 B.C.) with the use of the wheel and lubricants to reduce friction in translational motion [2]. Today, friction is considered a part of the wider field *tribology* derived from the Greek word *Tribos* meaning “rubbing” and includes the science of friction, wear and lubrication [2]. The most compelling motivation to study tribology is ultimately to gain full control of friction and wear for various technical applications. Especially, reducing friction is of great interest as this has tremendous advantages for energy efficiency. It has been reported that tribological problems have a significant potential for economic and environmental improvements [3]:

“On global scale, these savings would amount to 1.4% of the GDP annually and 8.7% of the total energy consumption in the long term.” [4].

On the other hand, the reduction of friction is not the only sensible application for tribological studies. Controlling frictional properties, besides minimization, might be of interest in the development of a grasping robot where finetuned object handling is required. While achieving a certain “constant” friction response is readily obtained through appropriate material choices, we are yet to unlock the full capabilities to alter friction dynamically on the go. One example from nature inspiring us to think along these lines are the gecko feet. More precisely, the Tokay gecko has received a lot of attention in scientific studies aiming to unravel the underlying mechanism of its “toggable” adhesion properties. Although geckos can produce large adhesive forces, they retain the ability to remove their feet from an attachment surface at will [5]. This makes the gecko able to achieve a high adhesion on the feet when climbing a vertical surface while lifting them for the next step remains relatively effortless. For a grasping robot, we might consider an analog frictional concept of a surface material that can change from slippery to rough on demand depending on specific tasks; Slippery and smooth when interacting with people and rough and firmly gripping when moving heavy objects.

In recent years an increasing amount of interest has gone into the studies of the microscopic origin of friction, due to the increased possibilities in surface preparation and the development of nanoscale experimental methods. Nano-friction is also of great concern for the field of nano-machining where the frictional properties between the tool and the workpiece dictate machining characteristics [3]. With concurrent progress in computational capacity and development of Molecular Dynamics (MD), numerical investigations serve as an invaluable tool for getting insight into the nanoscale mechanics associated with friction. This simulation-based approach can be considered as a “numerical experiment” enabling us to create and probe a variety of high-complexity systems which are still out of reach for modern experimental methods.

In materials science such MD-based numerical studies have been used to explore the concept of so-called *metamaterials* where material compositions are designed meticulously to enhance certain physical properties [6–

[11]. This is often achieved either by intertwining different material types or removing certain regions completely. In recent papers by Hanakata et al. [6, 7] numerical studies have showcased that the mechanical properties of a graphene sheet, yield stress and yield strain, can be altered through the introduction of so-called *kirigami* inspired cuts into the sheet. Kirigami is a variation of origami where the paper is cut additionally to being folded. While these methods originate as an art form, aiming to produce various artistic objects, they have proven to be applicable in a wide range of fields such as optics, physics, biology, chemistry and engineering [12]. Various forms of stimuli enable direct 2D to 3D transformations through folding, bending, and twisting of microstructures. While original human designs have contributed to specific scientific applications in the past, the future of this field is highly driven by the question of how to generate new designs optimized for certain physical properties. However, the complexity of such systems and the associated design space make for seemingly intractable problems ruling out analytic solutions.

Earlier architecture design approaches such as bioinspiration, looking at gecko feet for instance, and Edisonian, based on trial and error, generally rely on prior knowledge and an experienced designer [9]. While the Edisonian approach is certainly more feasible through numerical studies than real-world experiments, the number of combinations in the design space rather quickly becomes too large for a systematic search, even when considering the computation time on modern-day hardware. However, this computational time constraint can be relaxed by the use of machine learning (ML) which has proven successful in the establishment of a mapping from the design space to physical properties of interest. This gives rise to two new styles of design approaches: One, by utilizing the prediction from a trained network we can skip the MD simulations altogether resulting in an *accelerated search* of designs. This can be further improved by guiding the search accordingly to the most promising candidates, for instance, as done with the *genetic algorithm* based on mutation and crossing of the best candidates so far. Another more sophisticated approach is through generative methods such as *Generative Adversarial Networks* (GAN) or diffusion models with the latter being used in state-of-the-art AI systems such as OpenAI's DALL-E2 or Midjourney [SOURCE?](#). By working with a so-called *encoder-decoder* network structure, one can build a model that reverses the prediction process. That is, the model predicts a design from a set of physical target properties. In the papers by Hanakata et al both the *accelerated search* and the *inverse design* approach was proven successful to create novel metamaterial kirigami designs with the graphene sheet.

Hanakata et al attribute the variety in yield properties to the non-linear effects arising from the out-of-plane buckling of the sheet. Since it is generally accepted that the surface roughness is of great importance for frictional properties it can be hypothesized that Kirigami-induced out-of-plane buckling can also be exploited for the design of frictional metamaterials. For certain designs, we might hope to find a relationship between the stretching of the sheet and frictional properties. If significant, this could give rise to an adjustable friction behavior beyond the point of manufacturing. For instance, the grasping robot might apply such a material as artificial skin for which stretching or relaxing of the surface could result in a changeable friction strength.

In addition, the Kirigami graphene properties can be explored through a potential coupling between the stretch and the normal load, through a nanomachine design, with the aim of altering the friction coefficient. This invites the idea of non-linear friction coefficients which might in theory also take on negative values. The latter would constitute a rarely found property which is mainly found for the unloading phase of adhesive surfaces [13] or for the loading phase of particular heterojunction materials [14, 15].

To the best of our knowledge, Kirigami has not yet been implemented to alter the frictional properties of a nanoscale system. However, in a recent paper by Liefferink et al. [16] it is reported that macroscale kirigami can be used to dynamically control the macroscale roughness of a surface through stretching. They reported that the roughness change led to a changeable frictional coefficient by more than one order of magnitude. This supports the idea that Kirigami designs can be used to alter friction, but we believe that taking this concept to the nanoscale regime would involve a different set of underlying mechanisms and thus contribute to new insight in this field.

1.2 Goals

In this thesis, we investigate the possibility to alter the frictional properties of a graphene sheet through the application of Kirigami-inspired cuts and stretching of the sheet. With the use of molecular dynamics (MD) simulations, we evaluate the frictional properties of various Kirigami designs under different physical conditions. With the use of machine learning (ML), we perform an accelerated search of designs to explore new designs. The main goals of this thesis can be summarized as follows.

1. Design an MD simulation procedure to evaluate the frictional properties of a Kirigami graphene sheet under specified physical conditions.
2. Develop a numerical framework for creating various Kirigami designs, both by seeking inspiration from macroscale designs and by the use of a random walk based algorithm.
3. Investigate the frictional behavior under varying load and stretch for different Kirigami designs.
4. Develop and train an ML model to predict the MD simulation result and perform an accelerated search of new designs for the scope of optimizing certain frictional properties.

1.3 Contributions

What did I actually achieve [Include Githib link](#)

1.4 Thesis structure

In Part I: Background Theory, we cover the theoretical background related to Friction (Chapter 2), Molecular Dynamics (??) and Machine Learning (??).

In Chapter 2: Friction, we introduce the most relevant theoretical concepts of friction through a division by scale: Macroscale (Sec. 2.2), Microscale (Sec. 2.3) and nanoscale (Sec. 2.4). We emphasize the nanoscale since this is of the most importance for our study. This is followed by a summary of relevant experimental and numerical results Sec. 2.5 and a more formal specification of our research questions (Sec. 2.6).

In ??: Molecular Dynamics, we introduce the main concepts related to the simulations used in this thesis. The main parts involve a description of the potentials used (??), the numerical solutions (??) and the modeling of temperature (??)

In ??: Machine Learning, we introduce the basics of machine learning through a general presentation of the neural network ?? followed by the convolutional network (??) which we will use in our study. Additionally, we discuss a strategy for choosing model hypertuning (??) and a simple approach for model prediction explanations (). Finally, we introduce a version of the genetic algorithm applicable for accelerated search based on a machine learning model (??).

In Part II: Simulations, we define our numerical procedure and present and discuss the main findings of this thesis.

In ??: System, we ...

In ??: Pilot study, we ...

In ??: XXX ...

In Chapter 3: XXX, ...

The thesis is summarized in Chapter 4

Additional figures are shown in ??, ?? and ?? [get appendix with only letter A., B. and C.](#)

Part I

Background Theory

Chapter 2

Friction

Since we aim for controlling frictional properties, we will review the relevant theoretical understanding of friction in this chapter. We limit ourselves to the tribological subcategory, wearless dry friction, meaning that we consider friction in the absence of lubricant and wear between the contacting surfaces. We will direct the review towards our system of interest which will serve as a basis for a formal definition of our research questions.

2.1 Friction across scales

Tribological systems span a wide range of time and length scales, from geological stratum layers involved in earthquakes [3] to atomistic processes, such as the gliding motion of nanoclusters or nanomotors [17]. This vast difference in scale leads to different dominant frictional mechanisms. At the macroscale, systems are typically subject to relatively high loads and sliding speeds, resulting in significant contact stress and wear. On the other hand, the micro-/nanoscale regime occupies the opposite domain operating under a relatively small load and sliding speed with negligible wear [3] [2, p. 5]. While macroscale friction is often reduced into a few variables such as load, material type, sliding speed and surface roughness, it is clear that the micro-/nanoscale friction cannot be generalized under such a simple representation. On the micro-/nanoscale the tribological properties are dominated by surface properties which will yield a more complex behavior of said variables and introduce an additional sensitivity to variables such as temperature, humidity and even sliding history. The works of Bhushan and Kulkarni [18] showed that the friction coefficient decreased with scale even though the materials used were unchanged. This reveals an intrinsic relationship between friction and scale as the contact condition is altered.

The phenomenological descriptions of macroscale friction cannot yet be derived from the fundamental atomic principles, and bridging the gap between different length scales in tribological systems remains an open challenge [17]. Hence, the following sections will be organized into macroscale (Sec. 2.2), microscale (Sec. 2.3) and nanoscale (Sec. 2.4) representing the theoretical understanding governing each scale regime. Realizing that the field of friction across all scales is a vastly broad topic, we will only introduce the most essential findings for each scale, while keeping a main focus on features associated with our system which takes place at the nanoscale.

2.2 Macroscale

Our working definition of the *macroscale* is everything on the scale of millimeters and above [19]. This represents the scale of visible objects and includes everything from the everyday interaction with an object to the geological systems.

2.2.1 Amontons' law

In order to start and keep a solid block moving against a solid surface we must overcome certain frictional forces F_{fric} [1]. The static friction force F_s corresponds to the minimum tangential force required to initiate the sliding while the kinetic friction force F_k corresponds to the tangential force needed to sustain such a sliding at a steady speed. The work of Leonardo da Vinci (1452–1519), Guillaume Amontons (1663–705) and Charles de Coulomb (1736–1806) all contributed to the empirical law, commonly known as *Amontons' law*, which serves as a common

base for macroscale friction. Amontons' law states that the frictional forces are entirely independent of contact area and sliding velocity. Instead, it relies only on the normal force F_N , acting perpendicular to the surface, and the material-specific friction coefficient μ as

$$F_{\text{fric}} = \mu F_N. \quad (2.1)$$

Notice that the term *normal force* is often used interchangeably with *load* and *normal load* although the load and normal load refer to the applied force that pushes the object into the surface, whereas the normal force is the reaction force acting from the surface on the object. In equilibrium, these forces are equal in magnitude and opposite in direction. and hence we will not make a distinction between these terms. On the same note, we point out that the frictional force is different from a conventional force which in the Newtonian definition acts on a body from the outside and makes it accelerate [20]. Rather than being an independent external force the friction force is an internal *reaction* force opposing the externally applied "sliding" force.

The friction coefficient μ is typically different for the cases of static (μ_s) and kinetic (μ_k) friction, usually both with values lower than one and $\mu_s \geq \mu_k$ in all cases [1, p. 6]. The friction coefficient is taken to be a constant defined by either [20]

$$\mu_1 = \frac{F_{\text{fric}}}{F_N}, \quad (2.2a) \quad \text{or} \quad \mu_2 = \frac{dF_{\text{fric}}}{dF_N}. \quad (2.2b)$$

The first definition Eq. (2.2a) requires zero friction at zero load, i.e. $F_{\text{fric}} = 0$ at $F_N = 0$, while the second definition Eq. (2.2b) allows for a finite friction force at zero load as the coefficient is defined by the slope of the $F_{\text{fric}}-F_N$ -curve. The consequences of these definitions are illustrated in Fig. 2.1, for selected $F_{\text{fric}}-F_N$ -curves in Fig. 2.1a and corresponding friction coefficients in Fig. 2.1b and Fig. 2.1c. For adhesive contacts, the friction force will not be zero under zero load (red curve: Linear + shift) which can be mitigated by adding an extra constant to Eq. (2.1) [20]. Using Eq. (2.2a) for adhesive contacts would make the friction coefficient diverge for decreasing load as illustrated in Fig. 2.1b. Thus, we find the second definition Eq. (2.2b) more robust and versatile. This also allows for a better interpretation of the friction coefficient in the case where friction depends non-linearly on load (Purple curve in Fig. 2.1).

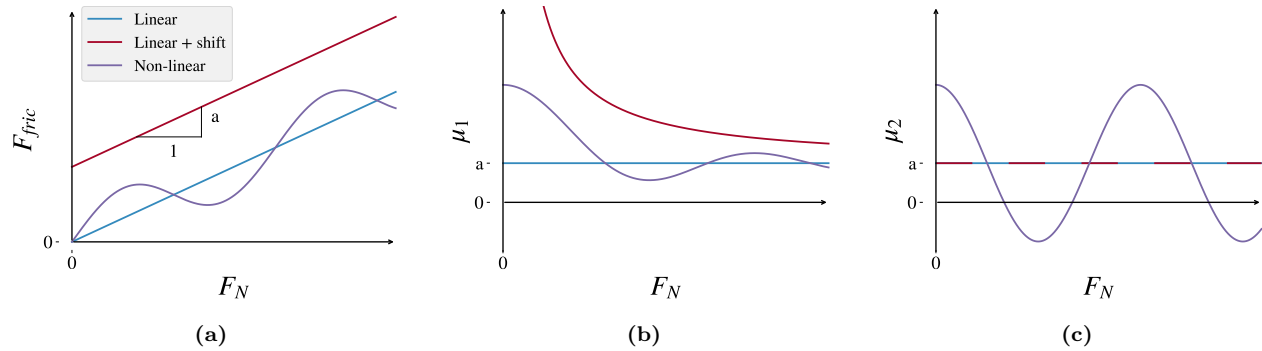


Figure 2.1: CAPTION

Amontons' law represents the behavior relatively accurately for many surfaces in contact, involving both dry and lubricated, ductile and brittle and rough and smooth surfaces (as long as they are not adhesive) under a variety of conditions [20]. But it has its limitations. For instance, at low velocities, Amontons' model breaks down due to thermal effects, and for high velocities due to inertial effects [1, pp. 5–6]. Additionally, static friction depends on the so-called contact history, with increasing static friction as the logarithm of time in stationary contact [21].

In cases where Amontons' law breaks down, we might still use the conceptual definition of the friction coefficient as defined by (Eq. (2.2b)). Especially, in the context of achieving negative friction coefficients (in certain load ranges), we would refer to this definition, since Eq. (2.2a) would imply a truly unphysical situation of the frictional force acting in the same direction as the sliding motion. This would accelerate the object indefinitely¹.

¹You would most likely have a good shot at the Nobel Prize with that paper.

Due to the empirical foundation of Amontons' law, it does not provide any physical insight into the underlying mechanisms of friction. However, as we will later discuss in more detail, we can understand the overall phenomena of friction through statistical mechanics by the concept of *equipartition of energy* [17]. A system in equilibrium has its kinetic energy uniformly distributed among all its degrees of freedom. When a macroscale object is sliding in a given direction it is clearly not in equilibrium since one of its degrees of freedom carries considerably more kinetic energy. Thus, the system will have a tendency to transfer kinetic energy to the remaining degrees of freedom in the form of heat dissipating to the surroundings and making the object slow down if not continuously driven forward by an external energy source. Hence, we can understand the overall concept of friction simply as the tendency of going toward equilibrium energy equipartitioning among many interacting degrees of freedom [17]. From this point of view, it is clear that friction is an inevitable part of contact physics, but even though friction cannot be removed altogether, we are still capable of manipulating it in useful ways.

The attentive reader might point out that we have already moved the discussion into the microscopic regime as *statistical mechanics* generally aim to explain macroscale behavior by microscopic interactions. In fact, this highlights the necessity to consider smaller scales in order to achieve a more fundamental understanding of friction.

We note that more advanced macroscale models for friction exist, for instance, the *earthquakelike* (EQ) model, also known as the *spring-and-block* model or the *multi-contact* model [Mani 2016] developed by Burridge and Knopoff [22]. This has been used in many studies of earthquake friction [23] and similar schemes have since been used to model the failure of fiber bundles and faults [24, 25]. Also, *rate and state* models have been used for earthquake modeling [26].

2.3 Microscopic scale

Going from a macro- to a microscale perspective, at a length scale on the order 10^{-6} m, it was realized that most surfaces are in fact rough [27]. The contact between two surfaces consists of numerous smaller contact points, so-called *asperities*, which form junctions due to contact pressure and adhesion as visualized in Fig. 2.2 [3]. In the macroscale perspective of Amonton's law, we refer to time- and space-averaged values, i.e. the apparent contact area and the average sliding speed [20]. However, microscopically we find the real contact area to be much smaller than the apparent area [3], and the shearing motion of local microjunctions to happen at large fluctuations rather than as one synchronized movement throughout the surface.

It is generally accepted that friction is caused by two mechanisms: Mechanical friction and chemical friction [3]. Mechanical friction is the “plowing” of the surface by hard particles or said asperities with an energy loss attributed to deformations of the asperity. While plastic deformations, corresponding to wear, gives rise to an obvious attribution for the energy loss, elastic deformations are also sufficient in explaining energy loss due to phonon excitations. The assumption of plastic deformations has been criticized as this is theorized only to be present at the beginning of a surface contact while it is negligible for prolonged or repeated contacts [28]. That is, when machine parts slide against each other for millions of cycles, the plastic deformation would only take place at the beginning for which the system then reaches a steady state with only elastic deformations. The chemical friction arises from adhesion between microscopic contacting surfaces, with an energy loss attributed to the breaking and forming of bonds. What kind of bonds

2.3.1 Asperity theories

Asperity theories have their foundations in the adhesion model proposed by Bowden and Tabor [29] which is based on the fundamental reasoning that friction is governed by the adhesion between two surfaces [30]. Adhesion is proportional to the real contact area defined by asperity junctions and interfacial shear strength τ between such contacting junctions. For an asperity contact area A_{asp} we get a true contact area $\sum A_{\text{asp}}$ leading to

$$F_{\text{fric}} = \tau \sum A_{\text{asp}}.$$

Note that this is still compatible with Amontons' law in Eq. (2.1) by having a linear relationship between the real contact area and the applied load. In fact, this is exactly how the theoretical model explains the friction dependency of load. By increasing the normal load it is hypothesized that the real contact area will increase as

the asperity tips are deformed (plastically or elastically) into broader contact points as visualized qualitatively in Fig. 2.2.

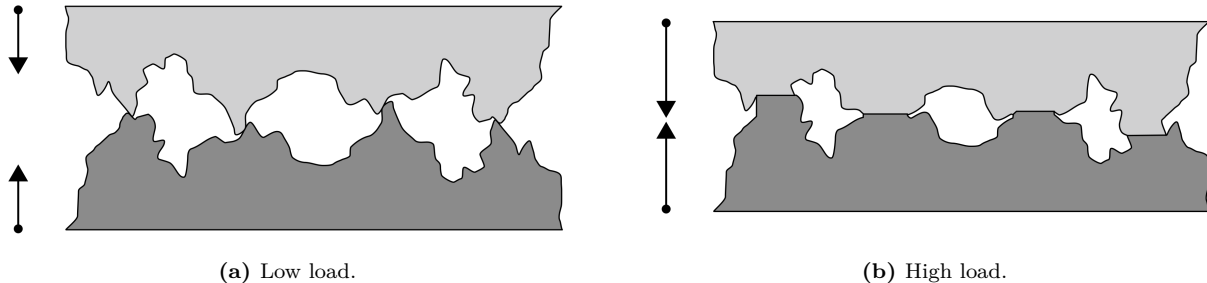


Figure 2.2: Qualitative illustration of the microscopic asperity deformation under increasing load from frame (a) to (b) [31]. While this figure seemingly portrays plastic deformation the concept of increased contact area under increased load applies to elastic deformation as well.

Many studies have focused on single asperity contacts to reveal the relationship between the contact area and load [32–34]. By assuming perfectly smooth asperities, with radii of curvature from micrometers all the way down to nanometers, continuum mechanics can be used to predict the deformation of asperities as load is applied. A model for non-adhesive contact between homogenous, isotropic, linear elastic spheres was first developed by Hertz [35], which predicted $A_{\text{asp}} \propto F_N^{2/3}$. Later adhesion effects were included in a number of subsequent models, including Maugis-Dugdale theory [36], which also predicts a sublinear relationship between A_{asp} and F_N . Thus, the common feature of all single-asperity theories is that A_{asp} is a sublinear function of F_N , leading to a similar sublinear relationship for $F_{\text{fric}}(F_N)$, which fails to align with the macroscale observations modeled by Amontons' law (eq. (2.1)).

Concurrently with single-asperity studies, roughness contact theories are being developed [37–40] to bridge the gap between single asperities and macroscopic contacts [27]. A variety of multi-asperity theories has attempted to combine single asperity mechanics by statistical modeling of the asperity height and spatial distributions [28]. This has led to partial success in the establishment of a linear relationship between A_{asp} and F_N . Unfortunately, these results are restricted in terms of the magnitude of the load and contact area, where multi-asperity contact models based on the original ideas of Greenwood and Williamson [39] only predicts linearity at vanishing low loads, or Persson [38] which predicts linearity for more reasonable loads but only up to 10–15 % of the macroscale contact area. However, as the load is further increased all multi-asperity models predict the contact area to fall into the sublinear dependency of normal force as seen for single asperity theories as well [28].

2.4 Nanoscale — Atomic scale

Going from a micro- to a nanoscale, on the order of 10^{-9} m, it has been predicted that continuum mechanics will start to break down [41] due to the discreteness of individual atoms. In a numerical MD study by Mo et al. [27], considering asperity radii of 5–30 nm, it has been shown that the asperity area A_{asp} , defined by the circumference of the contact zone, is sublinear with F_N . This is accommodated by the observation that not all atoms within the circumference make chemical contact with the substrate. By modeling the real contact area $A_{\text{real}} = N A_{\text{atom}}$, where N is the number of atoms within the range of chemical interaction and A_{atom} the associated surface area for a contacting atom, they found a consistent linear relationship between friction and the real contact area. Without adhesive forces, this leads to a similar linear relationship $F_{\text{fric}} \propto F_N$, while adding van der Waals adhesion to the simulation gave a sublinear relationship matching macroscale single asperity theory, even though the $F_{\text{fric}} \propto A_{\text{real}}$ was maintained. This result emphasizes that the predictions of continuum mechanics might still apply at the nanoscale and that the contact area can be expected to play an important role for nanoscale asperity contacts. It is simply the definition of the contact area that changes when transitioning from micro- to nanoscale.

While the study by Mo et al. [27] considers a single asperity on a nanoscale, some models take this even further to what we will denote as the atomic scale. This final leap is motivated by the fact that our system of interest, an atomically flat graphene sheet imposed on a flat silicon substrate, lacks the presence of nanoscale

asperities in its initial uncut undeformed state. In the lack of noteworthy structural asperities, friction can instead be modeled as a consequence of the “rough” potential laid out by the atomic landscape. A series of so-called *reduced-order* models build on a simplified system of atomic-scale contacts based on three essential parts: 1) A periodic potential modeling the substrate as a rigid crystalline surface. 2) An interacting particle, or collection of particles, placed in the potential. 3) A moving body, moving at a steady speed, connected to the particles through a harmonic spring. In figure Fig. 2.3 three of the most common 1D models are displayed which we will address in the following sections. The time-honored Prandtl-Tomlinson (PT) model describes a point-like tip sliding over a space-periodic fixed crystalline surface with a harmonic coupling to the moving body. This is analog to that of an experimental cantilever used for Atomic Force Microscopy which we will introduce in more detail in Sec. 2.4.5.1. Further extensions were added in the Frenkel-Kontorova (FK) model by substituting the tip with a chain of harmonically coupled particles dragged from the end, and finally combined in the Frenkel-Kontorova-Tomlinson (FKT) with the addition of a more rigorous harmonic coupling between the moving body and each of the atoms in the chain. While these models cannot provide the same level of detail as atomistic simulations such as MD they enable investigation of atomic friction under most conditions, some of which are inaccessible to MD [42]. This makes these models an appropriate tool for investigating individual parameters and mechanisms governing friction.

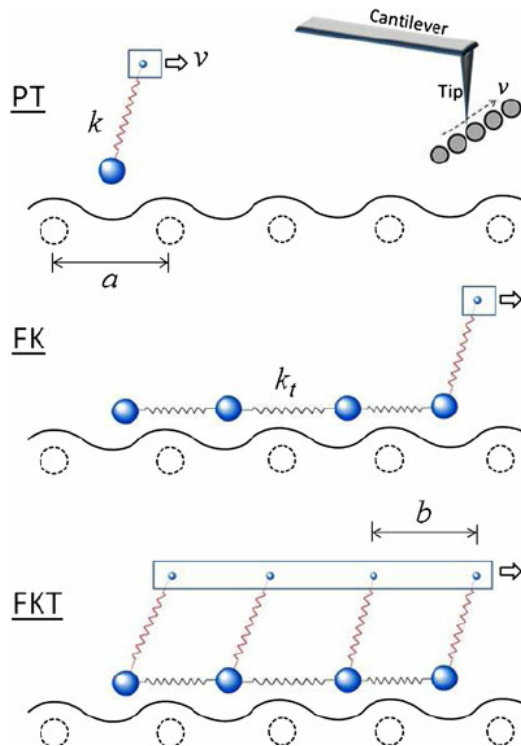


Figure 2.3: Temporary figure from [42]. Be careful to align the notation on the figures with the text later on.

2.4.1 Prandtl–Tomlinson

The Prandtl–Tomlinson model (PT) considers a 1D simplification of the frictional system as a single ball-tip sliding along the rigid substrate as shown in Fig. 2.3. The tip is coupled harmonically to a support moving at a constant speed which drives the tip forward. The interaction between the tip and the substrate is modeled as a sinusoidal corrugation potential mimicking the periodicity found in a crystalline substrate. We will consider Prandtl–Tomlinson model with added thermal activation as proposed by Gnecco et al. [43]. For the theoretical foundation of this section, we generally refer to [42]. The potential energy for the tip at position x for time t is given as

$$V(x, t) = \frac{1}{2}K(vt - x)^2 - \frac{1}{2}U_0 \cos\left(\frac{2\pi x}{a}\right). \quad (2.3)$$

The first term describes the harmonic coupling with spring constant K , between the tip at position x and the moving body at position vt , given by its constant speed v . The second term describes the corrugation potential with amplitude U_0 and period a representing the lattice spacing of the substrate. The dynamics of the tip can be described by the Langevin equations

$$m\ddot{x} + m\mu\dot{x} = -\frac{\partial V(x, t)}{\partial x} + \xi(t), \quad (2.4)$$

Match notation with later use.

where m is the mass of the tip, μ the viscous friction and $\xi(t)$ the thermal activation term. The equation is solved for tip position x and the friction force is retrieved as the force acting on the moving body

$$F_{\text{fric}} = K(vt - x).$$

The governing equation Eq. (2.4) belongs to a family of stochastic differential equations composed of both deterministic dynamics and stochastic processes. In this case, the deterministic term is the viscous friction, $m\mu\dot{x}$, to resist the movement of the tip and the force acting from the corrugation potential. The stochastic term is a random force field modeling thermal noise according to the Fluctuation-dissipation relation. Thus, there is no single path but rather multiple paths the tip can take. While the Langevin equations is one of the most common ways to handle thermal activation other methods exist to solve this problem such as Monte Carlo sampling methods. We omit the numerical scheme for the solving of the Langevin equations here and refer instead to a more in-depth discussion of the Langevin equations regarding the MD simulations in ??.

2.4.1.1 Thermal activation

The solving of the Langevin equations, as opposed to Newton's equation of motion, introduces thermal effects to the system. Generally, when the energy barrier comes close to $k_B T$ (0.026 eV at room temperature) thermal effects can not be neglected. In the case of a single asperity contact the energy barrier is on the order 1 eV which makes thermal activation significant [42]. Due to the moving body traveling at a constant speed, the potential energy will increase steadily. Without any temperature, $T = 0$, the slip will only occur when the energy barrier between the current potential well (i) and the adjacent (j) is zero $\Delta V_{i \rightarrow j} = 0$. However, in the presence of temperature, we get thermal activation, meaning that the tip can slip to the next potential well sooner $\Delta V_{i \rightarrow j} > 0$. Provided that the sliding speed is slow enough (Elaborate) the transition rate κ for a slip from the current to the next well is given by

$$\kappa = f_0 e^{-\Delta V/k_B T}, \quad (2.5)$$

with ΔV being the energy barrier and f_0 the attempt rate. The attempt rate following Kramer's rate theory [44] is related to the mass and damping of the system and can be thought of as the frequency at which the tip "attempts" to overcome the barrier. Notice that Eq. (2.5) resembles a microstate probability in the canonical ensemble with f_0 in place of the inverse partition function Z^{-1} which provides an additional interpretation of f_0 . The probability p_i that the tip occupies the current well i relative to the adjacent well j , as illustrated in Fig. 2.4 is governed by

$$\frac{dp_i}{dt} = -\kappa_{i \rightarrow j} p_i + \kappa_{j \rightarrow i} p_j.$$

This probability is related to temperature, speed and mass [42].

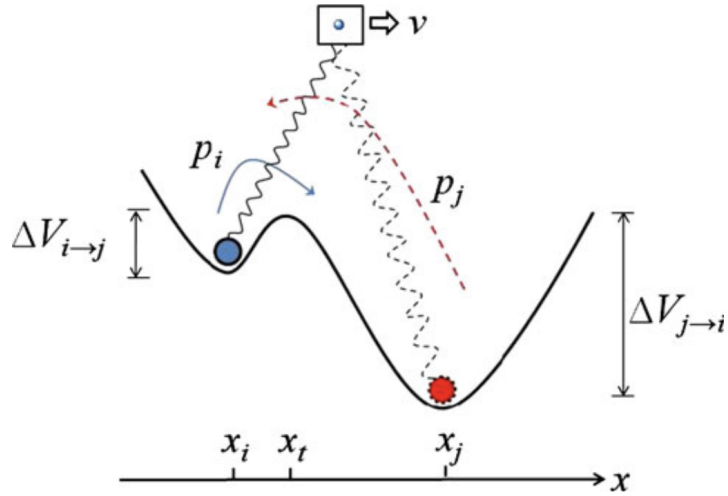


Fig. 3 An illustration of slip between two adjacent energy minima. p_i is the probability of the tip residing in the current potential well, i , where the energy barrier is $\Delta V_{i \rightarrow j}$. p_j is the probability of the tip residing at the next minima, j , where $\Delta V_{j \rightarrow i}$ is the corresponding energy barrier

Figure 2.4: [Temporary] figure from [42]

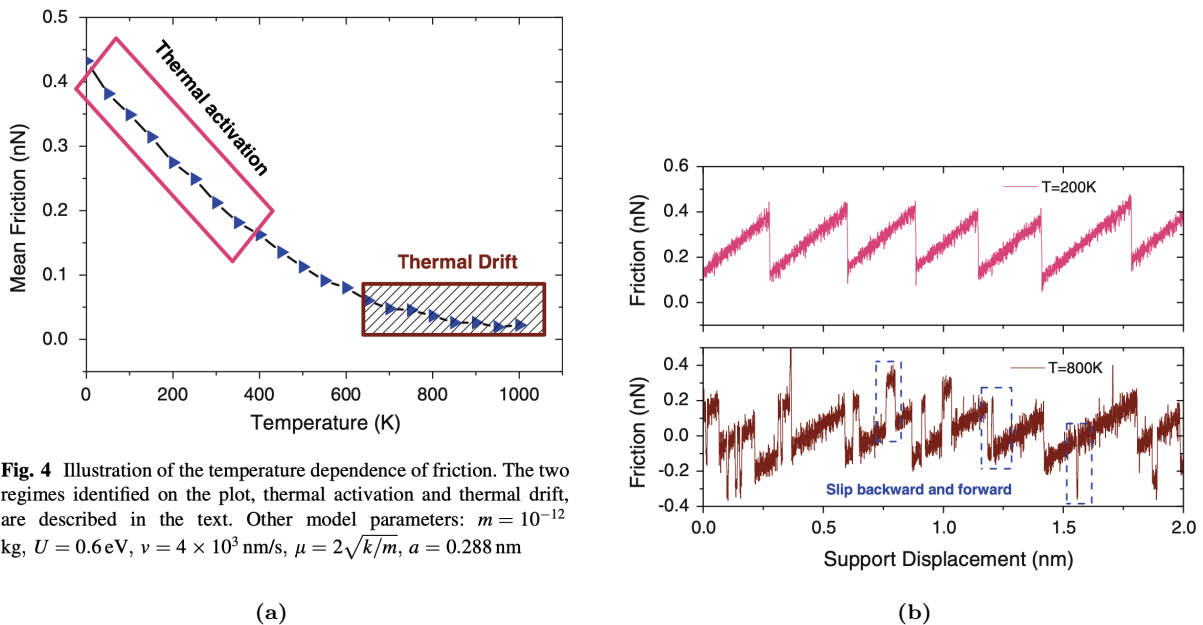


Fig. 4 Illustration of the temperature dependence of friction. The two regimes identified on the plot, thermal activation and thermal drift, are described in the text. Other model parameters: $m = 10^{-12}$ kg, $U = 0.6$ eV, $v = 4 \times 10^3$ nm/s, $\mu = 2\sqrt{k/m}$, $a = 0.288$ nm

Figure 2.5: [Temporary] figures from [42]

Generally, there exist two temperature regimes in the model: *Thermal activation* at low temperatures and *thermal drift* at high temperatures as shown in Fig. 2.5. At lower temperatures, the system is subject to standard thermal activation with $\Delta V_{j \rightarrow i} \gg \Delta V_{i \rightarrow j}$ resulting in $\kappa_{j \rightarrow i} \ll \kappa_{i \rightarrow j}$. Effectively, this inhibits any backward slip

and we get

$$\frac{dp_i}{dt} = -\kappa_{i \rightarrow j} p_i,$$

which makes the relationship between friction, temperature and speed follow Sang et al.'s prediction [45]

$$F = F_c - \left| \beta k_B T \ln \left(\frac{v_c}{v} \right) \right|^{2/3}, \quad v_c = \frac{2f_0 \beta k_B T}{3C_{\text{eff}} \sqrt{F_c}}, \quad (2.6)$$

where F_c is the maximum friction at $T = 0$, v_c a critical velocity, f_0 is the attempt rate, C_{eff} the effective stiffness, and β a parameter determined by the shape of the corrugation well. Eq. (2.6) characterizes the decrease in friction with temperature in the thermal activation regime, shown in Fig. 2.5a at low temperature. This corresponds with the assumption of only forward slips, as seen in the force trace shown in Fig. 2.5a. When the temperature is high enough for the system to be consistently close to thermal equilibrium, it enters the regime of thermal drift [46]. This regime transition can be understood through a comparison between two time scales: The time it takes for the moving body to travel one lattice spacing $t_v = a/v$ and the average time for a slip to occur due to thermal activation $\tau = 1/\kappa = f^{-1} \exp(\Delta V/k_B T)$. If $t_v \gg \tau$ the system falls within the thermal drift regime, with slips both backward and forwards as shown in Fig. 2.5b, and the friction follows the prediction of Krylov et al. [46–48]

$$F \propto \frac{v}{T} e^{1/T}. \quad (2.7)$$

Notice that the friction dependence on sliding speed changes between the temperature regimes as well.

2.4.1.2 Sliding speed

In the thermal activation regime (low temperature) and at low speeds the friction relation follows Eq. (2.6) making friction scale logarithmically with speed. For higher speed, above the critical velocity $v > v_c$, if only thermal effects are considered, Eq. (2.6) predicts that friction will eventually saturate and come to a plateau at $F_{\text{fric}} = F_c$. This is illustrated in Fig. 2.6 with this prediction being represented by the dotted line. However, as given away by the figure, for higher speed the model will enter an athermal regime where the thermal effects are negligible compared to other contributions [49]. In the athermal regime the damping term $m\mu\dot{x}$ will dominate yielding $F_{\text{fric}} \propto v$. The athermal regime is often observed in reduced-models if the system is overdamped or at high speeds. This concept is related to MD simulations where the accessible speeds often fall into the athermal regime [50]. It is unclear how this affects real physical systems for which there exist more dissipation channels than just a single viscous term [51]. For the thermal drift regime at higher temperatures the linear relation $F_{\text{fric}} \propto v$ as given by Eq. (2.7).

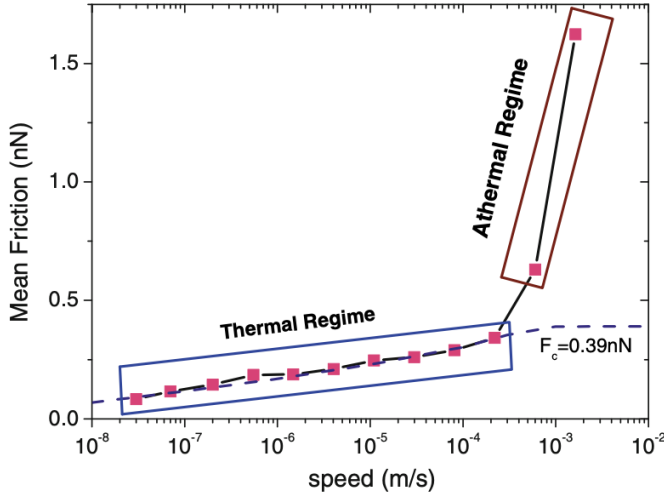


Fig. 6 Speed dependence of friction illustrating two different regimes. In the thermal regime, there is a logarithmic scaling of friction with speed, and in the athermal regime the friction is governed by the damping term such that $F \propto v$. The friction plateau ($F_c = 0.39$ nN) predicted by thermal activation is identified by the dashed line. Other model parameters: $m = 10^{-12}$ kg, $U = 0.6$ eV, $T = 300$ K, $v = 4 \times 10^3$ nm/s, $\mu = 2\sqrt{k/m}$, $a = 0.288$ nm

Figure 2.6: Temporary figure from [42]

2.4.1.3 Tip mass

The mass of the tip affects the dynamics due to a change of inertia, which changes the attempt rate f_0 . Smaller inertia leads to a larger attempt rate and vice versa. Effectively, this will affect the transition point for the temperature and speed regimes described previously. A smaller inertia, giving a larger attempt rate, will cause an earlier transition (i.e. at a lower temperature) to the thermal drift regime, and result in a later speed saturation such that it transitions to the athermal regime at a higher speed.

2.4.1.4 Friction Regimes: Smooth Sliding, Single Slip, and Multiple Slip

Stick-slip motion is a crucial instability mechanism associated with high energy dissipation and high friction. Thus, controlling the transition between smooth sliding and stick-slip is considered key to controlling friction. We can divide the frictional stick-slip behavior into three regimes: 1) Smooth sliding, where the tip slides smoothly on the substrate. 2) Single slip, where the tip stick at one potential well before jumping one lattice spacing to the next. 3) Multiple slip, where the tip jumps more than one lattice spacing for a slip event. The underlying mechanisms behind these regimes can be understood through static and dynamic contributions.

To understand the static mechanism we consider a quasistatic process for which temperature, speed and damping can be neglected and where we must have $\partial(V)/\partial x = 0$. This simplifies Eq. (2.3) to

$$\frac{\pi U_0}{a} \sin\left(\frac{2\pi x}{a}\right) \frac{2\pi}{a} = K(vt - x). \quad (2.8)$$

The friction regime is determined by the number of solutions x to Eq. (2.8). Only one solution corresponds to smooth sliding, two solutions to a single slip and so on. It turns out that the regimes can be defined by the parameter $\eta = 2\pi^2 U_0/a^2 K$ [52, 53] yielding transitions at $\eta = 1, 4.6, 7.79, 10.95, \dots$, such that $\eta \leq 1$ corresponds to smooth sliding, $1 < \eta \leq 4.6$ to a single slip and so on. These static derivations lay out the fundamental probabilities for being in one of the stick-slip regimes. Notice that increasing the spring constant K (stiff spring) will decrease the possibilities for stick-slip behavior. Similarly, the potential corrugation U_0 can be altered through an increased load of the system U_0 can be altered by an increasing load [54]

Considering the dynamics on top, one finds that damping, speed and temperature will affect this probability. High damping, equivalent to a high transfer of kinetic energy to heat, will result in less energy available for the slip events. This will make multiple slip less likely. By a similar argument, we find that increasing the speed will contribute to more kinetic energy which will increase the likelihood of multiple slip. Finally, the temperature will contribute to earlier slips, due to thermal activation, such that less potential energy can be accumulated and it will result in fewer multiple slip. The effects of damping, speed and temperature are illustrated for the force traces in Fig. 2.7

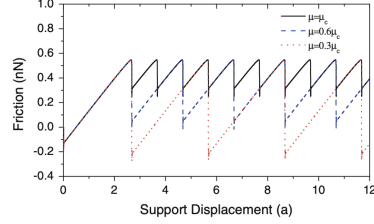


Fig. 9 The effect of damping on transitions between slip regimes where $\mu_c = 2\sqrt{k/m}$ is the critical damping coefficient. Single, double, and triple slip occur at $\mu = \mu_c$, $0.6 \mu_c$, and $0.3 \mu_c$, respectively. The abscissa has units of the lattice spacing a to facilitate identification of the transitions between single, double, and triple regimes. Other model parameters: $U = 0.6 \text{ eV}$, $T = 0 \text{ K}$, $v = 1 \mu\text{m/s}$, $m = 10^{-12} \text{ kg}$, $k = 1 \text{ N/m}$, $a = 0.288 \text{ nm}$

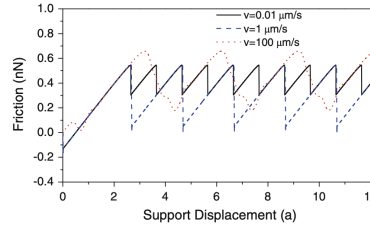


Fig. 10 The effect of sliding speed on transitions between slip regimes. Single, double, and triple slip occur at $v = 100$, 1 , and $0.01 \mu\text{m/s}$, respectively. Other model parameters: $U = 0.6 \text{ eV}$, $T = 0 \text{ K}$, $\mu = 0.8 \mu_c$, $m = 10^{-12} \text{ kg}$, $k = 1 \text{ N/m}$, $a = 0.288 \text{ nm}$

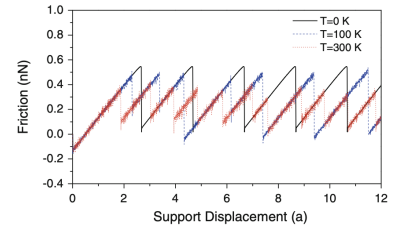


Fig. 11 The effect of temperature on transitions between slip regimes. Other model parameters: $U = 0.6 \text{ eV}$, $v = 1 \mu\text{m/s}$, $\mu = 0.6 \mu_c$, $m = 10^{-12} \text{ kg}$, $k = 1 \text{ N/m}$, $a = 0.288 \text{ nm}$

(a)

(b)

(c)

Figure 2.7: Temporary figure from [42]. Consider removing since the interpretation of smooth sliding might get a bit tricky.

2.4.2 Frenkel-Kontorova

The Frenkel-Kontorova (FK) model [55] extends the PT model by considering a chain of atoms in contrast to just a single particle (tip). This extension is useful for understanding the importance of the alignment between the atoms and the substrate, the so-called *commensurability*.

The standard (FK) model consists of a 1D chain of N classical particles of equal mass, representing atoms, interacting via harmonic forces and moving in a sinusoidal potential as sketched in Fig. 2.8 [17]. The Hamiltonian is

$$H = \sum_{i=1}^N \left[\frac{p_i^2}{2m} + \frac{1}{2}K(x_{i+1} - x_i - a_c)^2 + \frac{1}{2}U_0 \cos\left(\frac{2\pi x_i}{a_b}\right) \right], \quad (2.9)$$

where the atoms are labelled sequentially $i = 1, \dots, N$. The first term $p_i^2/2m$ represents the kinetic energy with momentum p_i and mass m . Often the effects of inertia are neglected, referred to as the static FK model, while the inclusion in Eq. (2.9) is known as the dynamic FK model [56]. The next term describes the harmonic interaction with elastic constant K , nearest neighbour distance $\Delta x = x_{i+1} - x_i$ and corresponding nearest neighbour equilibrium distance a_c . The final term represents the periodic corrugation potential, with amplitude U_0 and period a_b . By comparison to the potential used in the PT model Eq. (2.3), the only difference is the introduction of a harmonic coupling between particles in the chain as opposed to the moving body, and that we have not yet specified any force incentivizing sliding. Different boundary choices can be made where both free ends and periodic conditions give similar results. The choice of fixed ends however makes the chain incapable of sliding.

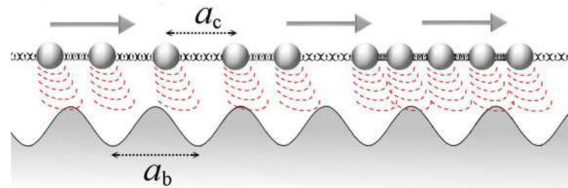


Figure 1. A sketch of the FK model, showing the two competing lengths: the average interparticle spacing and the lattice periodicity of the substrate.

Figure 2.8: Temporary figure from [17]

To probe static friction one can apply an external adiabatically increasing force until sliding occurs. This corresponds to the static FK model, and it turns out that the sliding properties are entirely governed by its topological excitations referred to as so-called *kinks* and *antikinks*

2.4.2.1 Commensurability

We can subdivide the frictional behavior in terms of commensurability, that is, how well the spacing of the atoms matches the periodic substrate potential. We describe this by the length ratio $\theta = a_b/a_c = N/M$ where M denotes the number of minima in the potential (within the length of the chain). A rational number for θ means that we can achieve a perfect alignment between the atoms in the chain and the potential minima, without stretching the chain, corresponding to a *commensurate* case. If θ is irrational the chain and substrate cannot fully align without some stretching of the chain, and we denote this as being *incommensurate*.

We begin with the simplest commensurate case of $\theta = 1$ where the spacing of the atoms matches perfectly with the substrate potential periodicity, i.e. $a_c = a_b$, $N = M$. The ground state (GS) is the configuration where each atom is aligned with one of the substrate minima. By adding an extra atom to the chain we would effectively shift some of the atoms, out of this ideal state, giving rise to a kink excitation. This leads to the case where two atoms will have to “share” the same potential corrugation as sketched in Fig. 2.10. On the other hand, removing an atom from the chain results in an antikink excitation where one potential corrugation will be left “atomless”. In order to reach a local minimum the kink (antikink) will expand in space over a finite length such that the chain undertakes a local compression (expansion). Notice that for low ratios of θ , fewer atoms than minima, the chain will not be able to fill each corrugation well in any case, meaning that commensurability can instead be thought of as whether the atoms are forced to deviate, by a lattice spacing, from the spacing otherwise dictated by the spring forces in-between. When applying a tangential force to the chain it is much easier for an excitation to move along the chain than it is for the non-excited atoms since the activation energy ϵ_{PN} for a kink/antikink displacement is systematically smaller (often much smaller) than the potential barrier U_0 . Thus, the motion of kinks (antikinks), i.e. the displacement of extra atoms (atom vacancies), is representing the fundamental mechanism for mass transport. These displacements are responsible for the mobility, diffusivity and conductivity within this model.

In the zero temperature commensurable case with an adiabatical increase in force, all atoms would be put into an accelerating motion as soon as the potential barrier energy is present. However, just as discussed for the PT model, thermal activations will excite the system at an earlier stage resulting in kink-antikink pairs traveling down the chain. For a chain of finite length, these often occur at the end of the chain running in opposite directions. This cascade of kink-antikink excitations is shown in Fig. 2.9. Notice, that for the 2D case, where an island (or flake) is deposited on a surface, we generally also expect the sliding to be initiated by kink-antikink pairs at the boundaries.

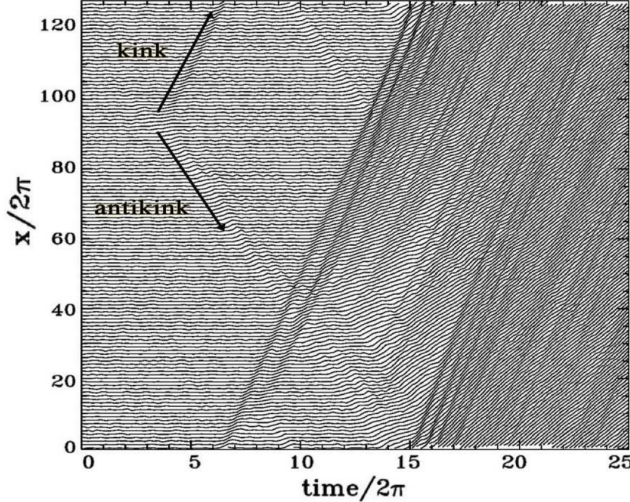


Figure 2. Time dependence of the atomic trajectories for the fully matched ($\theta = 1$) FK model at the (low-temperature) onset of depinning. Motion starts with the nucleation of a kink-antikink pair. The kink and the antikink depart in opposite directions cross the periodic boundary conditions, and collide quasielastically. A second kink-antikink pair forms in the wake of the initial kink. Further kink-antikink pairs are generated, with an avalanche-like increase of the kink-antikink concentration, eventually leading to a sliding state. Adapted from Ref. [21], Copyright (1997) by The American Physical Society.

Figure 2.9: Temporary figure from [17]

For the case of incommensurability, i.e. $\theta = a_b/a_c$ is irrational, the GS is characterized by a sort of “staircase” deformation. That is, the chain will exhibit regular periods of regions approximate commensurability separated by regularly spaced kinks or antikinks.



Figure 2.10: Temporary figure from [urlhttp://www.iop.kiev.ua/~obraun/myreprints/surveyfk.pdf](http://www.iop.kiev.ua/~obraun/myreprints/surveyfk.pdf) p. 14. Incommensurable case ($\theta = ?$) where atoms sit slightly closer than otherwise dictated by the substrate potential for which this regular result in a kink here seen as the presence of two atoms closely together in one of the potential corrugations.

The incommensurable FK model contains a critical elastic constant K_c , such that for $K > K_c$ the static friction F_s drops to zero, making the chain able to initiate a slide at no energy cost, while the low-velocity kinetic friction is dramatically reduced. This can be explained by the fact that the displacement occurring in the incommensurable case will yield just as many atoms climbing up a corrugation as there are atoms climbing down. For a big (infinite) chain this will exactly balance the forces making it non-resistant to sliding. Generally, incommensurability guarantees that the total energy (at $T = 0$) is independent of the relative position to the potential. However, when sliding freely, a single atom will eventually occupy a maximum of the potential, and thus when increasing the potential magnitude U_0 or softening the chain stiffness, lowering K , the possibility to occupy such a maximum disappears. This marks the so-called Aubry transition, at the critical elastic constant $K = K_c(U_0, \theta)$, where the chain goes from a free sliding to a *pinned* state with nonzero static friction. K_c is a discontinuous function of the ratio θ , due to the reliance on irrational numbers for incommensurability. The minimal value $K_c \simeq 1.0291926$ in units $[2U_0(\pi/a_b)^2]$ is achieved for the golden-mean ratio $\theta = (1 + \sqrt{5}/2)$. Notice that the pinning is provided despite translational invariance due to the inaccessibility to move past the energy

barrier which acts as a dynamical constraint. The Aubry transition can be investigated as a first-order phase transition for which power laws can be defined for the order parameter, but this is beyond the scope of this thesis.

The phenomena of non-pinned configurations are named *superlubricity* in tribological context. Despite the misleading name, this refers to the case where the static friction is zero while the kinetic friction is nonzero but reduced. For the case of a 2D sheet, it is possible to alter the commensurability, not only by changing the lattice spacing through material choice but also by changing the orientation of the sheet relative to the substrate. Dienwiebel et al. [57] have shown that the kinetic friction, for a graphene flake sliding over a graphite surface (multiple layers of graphene), exhibits extremely low friction at certain orientations as shown in Fig. 2.11. Here we clearly see that friction changes as a function of orientation angles with only two spikes of considerable friction force. This relates back to the concept of frictional regimes introduced through the simpler PT model, where the change in orientation affects the effective substrate potential. Merely from the static consideration, we found that lowering the potential amplitude U_0 will decrease the parameter $\eta = 2\pi^2 U_0/a^2 K$ shifting away from the regime of multiple slips towards smooth sliding associated with low friction. Such transitions will also be affected by the shape of the potential and corresponding 2D effects of the sliding path [42].

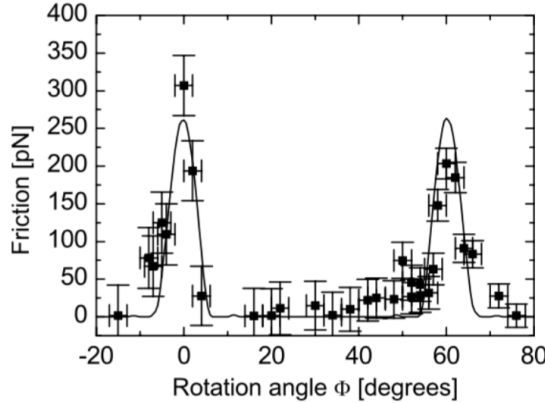


Fig. 6. Average friction force versus rotation angle Φ of the graphite sample around an axis normal to the sample surface. Two narrow peaks of high friction are observed at 0° and 61° , respectively. Between these peaks a wide angular range with ultra-low friction, close the detection limit of the instrument, is found. The first peak has a maximum friction force of 306 ± 40 pN, and the second peak has a maximum of 203 ± 20 pN. The curve through the data points shows results from a Tomlinson model for a symmetric 96-atom graphite flake sliding over the graphite surface (for details about the calculation see [39]).

Figure 2.11: **Temporary** figure from [57] showing superlubricity for incommensurable orientations between graphene and graphite. **temporary**

2.4.2.2 Velocity resonance

While many of the same arguments used for the PT model regarding velocity dependence for friction can be made for the FK model, the addition of multiple atoms introduces the possibility of resonance. In the FK model the kinetic friction is primarily attributed to resonance between the sliding induced vibrations and phonon modes in the chain [56]. The specific dynamics are found to be highly model and dimension specific, and even for the 1D case, this is rather complex. However, we make a simplified analysis of the 1D rigid chain case to showcase the reasoning behind the phenomena.

When all atoms are sliding rigidly with center of mass velocity v_{CM} the atoms will pass the potential maxima with the so-called *washboard frequency* $\Omega = 2\pi v_{CM}/ab$. For a weak coupling between the chain and the potential we can use the zero potential case as an approximation for which the known dispersion relation for the 1D

harmonic chain is given [58, p. 92]

$$\omega_k = \sqrt{\frac{4K}{m}} \left| \sin\left(\frac{k}{2}\right) \right|,$$

where ω_k is the phonon frequency and $k = 2\pi i/N$ the wavenumber with $i \in [N/2, N/2)$. Resonance will occur when the washboard frequency Ω is close to the frequency of the phonon modes ω_q in the chain with wavenumber $q = 2\pi a_c/a_b = 2\pi\theta^{-1}$ or its harmonics nq for $n = 1, 2, 3, \dots$ [59]. Thus, we can approximate the resonance center of mass speed as

$$\begin{aligned} n\Omega &\sim \omega_{nq} \\ n\frac{2\pi v_{CM}}{a_b} &\sim \sqrt{\frac{4K}{m}} \left| \sin\left(\frac{2n\pi\theta^{-1}}{2}\right) \right| \\ v_{CM} &\sim \frac{\sin(n\pi\theta^{-1})}{n\pi} \sqrt{\frac{Ka_b^2}{m}}. \end{aligned}$$

When the chain slides with a velocity around resonance speed, the washboard frequency can excite acoustic phonons which will dissipate to other phonon modes as well. At zero temperature, the energy will transform back and forth between internal degrees of freedom and center of mass movement of the chain. Without any dissipation mechanism this is theorized to speed up the translational decay [56]. However, as soon as we add a dissipation channel through the substrate, energy will dissipate from the chain to the substrate's degrees of freedom. This suggests that certain sliding speeds will exhibit relatively high kinetic friction while others will be subject to relatively low kinetic friction. Simulations of concentric nanotubes in relative motion (telescopic sliding) support this idea as it has revealed the occurrence of certain velocities at which the friction is enhanced, corresponding to the washboard frequency of the system [17], where the friction response was observed to be highly non-linear as the resonance velocities were approached.

The analysis of the phonon dynamics is highly simplified here, and a numerical study of the FK by Norell et al. [56] showed that the behavior was highly dependent on model parameter choices, but that the friction generally increased with velocity and temperature. Here the latter observation differs qualitatively from that of the PT model.

2.4.3 Frenkel-Kontorova-Tomlinson

A final extension of the atomic models worth mentioning here is the Frenkel-Kontorova-Tomlinson (FKT) model [60], which introduces a harmonic coupling of the sliding atom chain to the driving moving body, effectively combining PT and FK (see Fig. 2.3). This introduces more degrees of freedom to the model based on the intention of getting a more realistic connection between the moving body and the chain. Dong et al. carried out a numerical analysis using the 1D FKT model investigating the effect of chain length. They observed that the friction increased linearly with the number of atoms in the chain on a long-range, but certain lattice mismatch resulted in local non-linear relationships as shown in Sec. 2.4.3. Similarly, by extending the FKT model to 2D they were able to achieve a similar sensitivity to commensurability as observed experimentally by [57] (shown in Fig. 2.11) with the numerical result shown in Sec. 2.4.3. Besides a demonstration of the commensurability effect in 2D they also observed increasing friction with an increasing flake size. Combined, the 1D and 2D results support the idea of increasing friction with contact size although it might showcase non-linear behavior depending on commensurability.

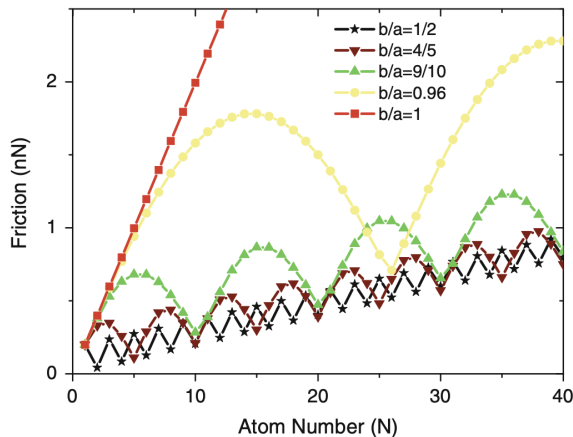


Fig. 21 Friction variation with the tip size N for different lattice mismatch b/a . $k = 5 \text{ N/m}$ and $k_t = 50 \text{ N/m}$ are used to obtain these results

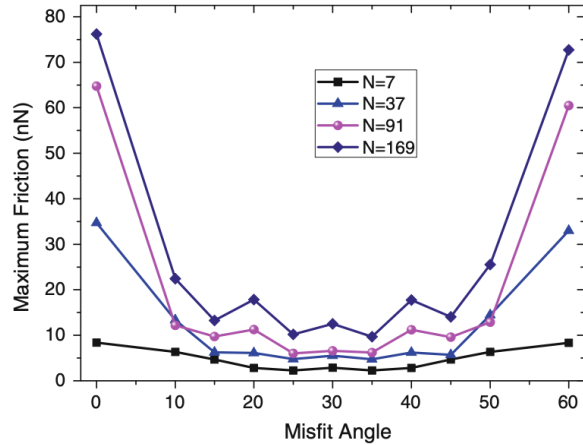


Fig. 23 The misfit angle dependence of friction with different tip sizes; $k_t = 50 \text{ N/m}$ and $k = 10 \text{ N/m}$. The $N = 7$ curve corresponds to the model illustrated in Fig. 22

(a) [Temporary] figure from [42]

(b) [Temporary] figure from [42]

2.4.4 Shortcomings of atomic models

To-DO: Shortcomings of PT-based reduced-models

- Assumes a rigid substrate with a simplified potential shape.
- Energy dissipation is added through a viscous term $-m\mu\dot{x}$ being the only dissipation channel available. Does not capture a more complex real-life electron and phonon dissipation. Taking phonon dissipation as an example there are many vibration modes ($3N$). This will affect the thermal activation derivation.
- The moving body is simplified as a constantly moving rigid body, while in fact this will also be subject to a more complex dynamic behavior.

2.4.5 Experimental procedures

Experimentally, the study of nanoscale friction is challenging due to the low forces on the scale of nano-newtons along with the difficulties of mapping the nano-scale topography of the sample. In contrast to numerical simulations, which provide full transparency regarding atomic-scale structures, sampling of forces, velocities and temperature, the experimental results are limited by the state-of-the-art experimental methods. To compare numerical and experimental results we address a few of the most relevant experimental methods.

2.4.5.1 Scanning Probe Microscopy

Scanning probe microscopy (SPM) includes a variety of experimental methods which is used to examine surfaces with atomic resolution [61, pp. 6-27]. This was originally developed for surface topography imaging, but today it plays a crucial role in nanoscale science as it is used for probe-sampling regarding tribological, electronic, magnetic, biological and chemical character. The family of methods involving the measurement of forces is generally referred to as *scanning force microscopies* (SFM) or for friction purposes *friction force microscopes* (FFM).

One such method arose from the *atomic force microscope* AFM, which consists of a sharp micro-fabricated tip attached to a cantilever force sensor, usually with a sensitivity below 1 nN all the way down to pN. The force is measured by recording the bending of the cantilever, either as a change in electrical conduction or more commonly, by a light beam reflected from the back of the cantilever into a photodetector [1, p. 183]. By adjusting the tip-sample height to keep a constant normal force while scanning across the surface, the AFM can be used to produce a surface topography map. By tapping the material (dynamic force microscopy) with

a sinusoidally vibrated tip the effects from friction and other disturbing forces can be minimized to produce an even clearer image (include example, preferably showing the surface structure of graphene). However, when scanning perpendicularly to the cantilever axis, one is also able to measure the frictional force as torsion of the cantilever. By having four quadrants in the photodetector (as shown in figure Fig. 2.13), one can simultaneously measure the normal force and friction force as the probes scan across the surface.

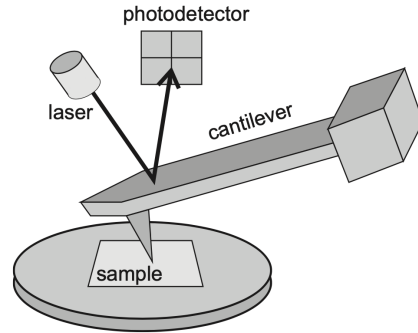


Figure 17.1 Schematic diagram of a beam-deflection atomic force microscope.

Figure 2.13: [Temporary] figure from [1, p. 184]

AFM can also be used to drag a nanoflake across the substrate as done by Dienwiebel et al. [57], where a graphene flake was attached to a FFM tip and dragged across graphite. Notice that this makes the normal loading concentrated to a single point on the flake rather than achieving an evenly distributed load.

2.4.5.2 Surface Force Apparatus

The Surface force apparatus SFA is based on two curved molecularly smooth surfaces brought into contact [1, p. 188]. The sample is placed in between the two surfaces as a lubricant film for which the friction properties can be studied by applying a tangential force to the surfaces.

2.5 Summary of previous results

Several studies have investigated the frictional behavior of graphene by varying different parameters such as normal force, sliding velocity, temperature, commensurability and graphene thickness [62]. In general, we find three types of relevant systems being studied: 1) An FFM type setup where the graphene, either resting on a substrate or suspended, is probed by an AFM tip scanning across the surface. 2) A SFA setup with the graphene “sandwiched” in between two substrate layers moving relative to each other using the graphene as a solid lubricant. 3) A graphene flake sliding on a substrate, either being dragged by an AFM tip or by more complex arrangements in numerical simulations. Considering that even the sharpest AFM tip will effectively put multiple atoms in contact with the sample, all methods are relatable to the study of nanoscale surface contacts. However, the FFM type is more reminiscent of asperity theory as we expect it to deform with increasing load, while the latter two are more aligned with the PT type models and our specific system of interest. Nonetheless, we will consider results across all three types of systems with the relevant studies summarized in Table 2.1 for convenience.

Table 2.1: Update multirow line span after completing the table...

System	Type	Year	Researcher	Materials	Keywords
FFM	Exp.	2007 [63]	Zhao et al.	Si ₃ N ₄ tip on graphite.	Temperature dependence
		2015 [64]	G. Paolicelli et al.	Si tip, graphene on SiO ₂ and Ni(111) substrate	Layers, load, shear strength
	Both	2019 [65]	Zhang et al.	Monolayer graphene	Straining sheet
		2019 [66]	Vazirisereshk et al.	Graphene, MoS ₂ and Graphene/MoS ₂ heterostructure	Low friction?
	Num.	2015 [67]	Yoon et al.	Si tip, graphene on SiO ₂	Stick-slip: tip size, scan angle, layer thickness, substrate flexibility
		2016 [68]	Li et al.	Si tip, graphene on a-Si substrate	Increasing layers
	SFA	2011 [69]	Wijn et al.	Graphene flakes between graphite	Rotational dynamics, superlubricity, temperature
		2012 [30]	H. J. Kim and D. E. Kim.	Carbon sheet	Corrugated nano-structured surfaces
Flake	Exp.	2005 [57]	Dienwiebel et al.	Graphene on graphite	Commensurability, superlubricity
		2013 [70]	Feng et al.	Graphene on graphite	Free sliding
	Num.	2009 [71]	Bonelli et al.	Graphene on graphite	Tight-binding, commensurability, load, flake size
		2012 [72]	Reguzzoni et al.	Graphene on graphite	Graphite thickness
		2014 [73]	Liu et al.	Graphene on graphite	Thickness, deformations, high speed
		2018 [74]	P. Zhu and Li	Graphene on gold	Flake size, commensurability
		2019 [75]	Zhang et al.	Graphene on diamond	Temperature, sliding angle, friction coefficient

One of the earliest tribological simulations of graphene was carried out by Bonelli et al. [71] in 2009 using a tight-binding method (excluding thermal excitations) to simulate a graphene flake on an infinite graphene sheet [62]. They implemented a FKT-like setup where each atom in the flake is coupled horizontally to a rigid support by elastic springs. They recovered the stick-slip behavior, which is also observed in FFM setups both experimentally [63, 65] and numerically [68, 74]. Moreover, they found an agreement with the qualitative observation that soft springs allow for a clean stick-slip motion while hard springs ($\sim 40 \text{ N/m}$) inhibited it, which also aligns with the PT model. In AFM and SFA experiments, the stick-slip motion tends to transition into smooth sliding when the speed exceeds $\sim 1 \mu\text{s}$ while in MD modeling the same transition is observed in the $\sim 1 \text{ m/s}$ region [17]. More precisely Liu et al. [73] findes the transistion MD simulations at 15 m/S. This 6-order-of-magnitude discrepancy has been largely discussed in connection to simplifying assumptions in MD simulations. On the other hand, the PT model qualitatively disagrees as it predicts smooth sliding for low speeds and stick-slip for high speeds. However, in an extension of the PT for the study of nanoscale rolling friction by Sircar and Patra [76], they found smooth sliding for high speeds.

Bonelli et al. [71] also found that commensurability, through orientation of the flake and the direction of sliding, had a great impact on the frictional behavior which generally aligns with the predictions of the FK and FKT models. They confirmed qualitatively the observation of superlubricity for certain incommensurable orientations which has been reported in experiments by Dienwiebel et al.[57] and further supported by experimental measurements of interaction energies by Feng et al. [70]. The importance of commensurability is also reported for MD simulations [69, 74, 75]. Bonelli et al. found the friction force and coefficient to be one order of magnitude higher than that of the experimental results which they attribute to the details of the numerical modeling. Generally, the experimental coefficients between graphite and most materials lie in the range of 0.08–0.18 [57].

While Dienwiebel et al. [57] reported a wide range of frictional forces from 28 ± 16 pN to 453 ± 16 pN with loads $\sim [-10, 20]nN$, the change in friction with applied load was as low as 0.05–0.4 % for the incommensurable orientations. When using the slope definition for the frictional coefficient Eq. (2.2b), this corresponds to a coefficient in the range of 0.0005–0.004. Bonelli et al. attribute the low dependency to a lacking change in contact area as the flake is loaded.

Furthermore, Bonelli et al. [71] found friction to decrease with increasing flake size which is also reported in MD simulations for graphene on gold [74]. Bonelli et al. mainly attribute this to boundary effects, but also note that the coupling to the support made for decreased rotational freedom as flake size was increased. Thus, they hypothesized that the decreased freedom led to the graphene taking a more forced path which is associated with a decreased stick-slip behavior. The general observation however, disagrees with the FK and FKT model which predicts the reverse; an increase in friction with increasing size.

An additional numerical study of monolayer islands of krypton on copper by Reguzzoni and Righi [77], supports the importance of commensurability regarding size effects, as they report that the effective commensurability increase drastically below a critical flake radius on the order of 10 Å. In a numerical study by Varini et al. [78], based on Kr islands adsorbed on Pb(111), this is further elaborated as they found that finite size effects are especially important for static friction due to a pinning barrier arising from the edge, preventing otherwise superlubricity due to incommensurability. They reported a relationship $F_s \sim A^{\gamma_s}$ not only sublinear, $\gamma_s < 1$, but also sublinear with respect to the island perimeter, $P \propto A^{1/2}$, by having $\gamma_s = 0.25$ for a hexagonal edge and $\gamma_s = 0.37$ when circular, indicating that only a subset of the edge is responsible for the pinning effect. This aligns with the general change in friction found by [74] for different flake geometries (square, triangle, circle). Additionally, Varini et al. found the edge pinning effect to decrease with increasing temperature as the edge energy barriers are reduced. Bringing all this together, the main picture forming is that flake size, which can be related to contact area, is affecting friction through a commensurability mechanism. If the flake is constrained in some way we might not observe the same dependency. While flake size nor contact area is easily measured in experimental FFM, Mo et al. [27] found in an MD simulation that friction is proportional to contact area for an indenting sphere on a nanoscale.

Evolution effects, or so-called friction strengthening, are also observed. That is, friction increases during the initial stick-slip cycles, which is observed experimentally by Zhang et al. [65] and numerically by Li et al. [68]. However, this is only found when having the graphene sheet resting on a substrate [65], as opposed to a suspended sheet. It is also found to diminish with an increasing number of graphene layers stacked (graphite) [68]. In the study by Li et al., they reported a general decrease in friction with an increasing number of layers which is found in other MD studies [67] and experimental studies as well [79, 80]. However, we also found an MD study reporting the opposite trend [72].

A few numerical studies investigate friction under mechanical deformations. Zhang et al. [65] found that straining a suspended graphene sheet will lower the kinetic friction. They attribute this to modulation of flexibility which consequently changes the local pinning capability of the contact interface. Liu et al. [73] carried out an MD simulation of high-speed (400 m/s) ballistic nanofriction of graphene on graphite. They found that a biaxial stretching of the graphitic substrate could be used to suppress frictional scattering and achieve persistent superlubricity. Another surface manipulating study was performed by H. J. Kim and D. E. Kim [30] who investigated the effects of corrugated nano-structured surfaces. The study revealed that corrugated surfaces with altered contact areas and structural stiffness could result in both increased or slightly decreased friction under certain load ranges. Altogether these studies highlight the importance of surface structure and mechanical conditions.

The friction dependency of normal load turns out to be a complex matter and has proven to be a highly system-dependent feature. As already mentioned, asperity theory mainly points to a sublinear relationship between friction and load, while the reduced-models point to a more intricate relationship through the change of the effective substrate potential which leads to an altering of the commensurability and the phonon dynamics. Experimentally rather different trends have been observed, although the majority agree on increasing friction with increasing load [1, p. 200]. For the graphene flake, Dienwiebel et al. [57] found a seemingly non-dependent relationship while FFM study by G. Paolicelli et al. [64] found a sublinear relationship matching the predictions of Maugis-Dugdale theory ($F_f \propto (F_N - F_{N,0})^{2/3}$). The discrepancy might be attributed to the difference in system type; A spherical tip indenting the graphene sheet as opposed to the atomic flatness of the graphene-graphite interface, which does not make for a changing contact area under load. However, numerical studies using a graphene-graphite interface still find both sublinear [71] and linear [65, 75] load dependencies.

In an experimental FFM study by Deng et al. it was discovered that the friction force kept increasing after unloading the probe tip from the graphite surface. This has been argued to be a more general phenomenon related to hysteresis in the adhesive interaction between two sliding bodies [81]. Following the slope definition for the friction coefficient, these results correspond to a negative friction coefficient. More recently, a negative friction coefficient has also been observed for the loading phase by Liu et al. [14] in an experimental study of the interface between graphite and muscovite mica heterojunction. With supporting numerical modeling this is attributed to “synergetic and nontrivial redistribution of water molecules at the interface”. Similar results are also reported numerically by [15] for graphite in contact with hexagonal boron nitride heterojunctions which is attributed to “load-induced suppression of the moiré superstructure out-of-plane distortions leading to a less dissipative interfacial dynamics”. Thus, the concept of a negative friction coefficient has been proven for the unloading phase of adhesive contacts and in the loading phase for a few systems.

The dependency of velocity is generally found to increase logarithmically with velocity in experimental AFM studies [1, p. 201] which match the low-velocity regime of the PT type models. At higher velocities, thermally activated processes are less important and friction becomes independent of velocity according to the PT model result Eq. (2.6) when ignoring the athermal regime. Saturation of the velocity dependency has been observed numerically for Si tips interacting with diamond, graphite and amorphous carbon surfaces respectively with scan velocities above $1 \mu\text{m/s}$ [82]. Guerra et al. [83], studying gold clusters on graphite using MD simulations, found a viscous friction response, friction being proportional to sliding velocity, in both low and high speed domains. However, thermal effects reversed as they found friction to decrease with increasing temperature at low speed (diffusive regime), but for high speed (ballistic regime) they found an increasing friction with temperature. In the MD simulations this crossover from ballistic to diffusive occurred between 10 and 1 m/s .

Regarding temperature itself, the general experimental trend is decreasing friction with increasing temperature as found by Zhao et al. [63] in a series of AFM graphene on graphite experiments yielding $F_{\text{fric}} \propto \exp(1/T)$. This agrees with the thermal drift regime of the PT model even though the exact temperature range does not agree. Moreover, Wijn et al. [69] found that friction commensurability can be lost at higher temperatures (above 200K) where they found a power law behavior $F_k \propto T^{-1.13 \pm 0.04}$. Numerically, Zhang et al. [75] found that friction increased with temperature, using a sliding speed of 10 m/s . Considering the findings of [83] this qualitative different behavior might be attributed to an MD related effect associated with the transition from low speed diffusive behavior as to high speed ballistic behavior.

From the review of previous results, we find several gaps and discrepancies in the description of friction provided by the reduced-models, MD simulations and experimental methods respectively. Some of the discrepancies can be attributed to the fact that different physical mechanisms are included in the numerical modeling. The reduced-models provides the simplest description while MD simulations are thought to capture a more complex behavior. On the other hand, we might also point differences in the studied systems as an important factor to consider. This regard the physical conditions such as sliding speed and temperature, but also higher level features concerning the mechanical properties of the system. For instance, the FFM based results consider an asperity-like system where the tip is expected to deform under loading, which gives rise to a change in contact area. This feature is lacking in the flat flake-/sheet-systems, and thus we might question the role of the contact area in these systems. More precisely, when inflicting an out-of-plane buckling through Kirigami cuts and stretching, the contact area is expected to decrease as well. From asperity theory we might simply hypothesize that friction will decrease during such a transition. However, as the system deforms we can also expect a modification of the commensurability, and the local loading which can be associated with radical changes in the frictional behavior associated with different stick-slip regimes. From the results of a non-Kirigami sheet under tension, we already see clues that the stretching will provide an reduction in friction without considering the contact area. Similar, the results from a corrugated nano surface also points to the fact that surface stiffness might play an important role as well.

2.6 Research questions

Based on the review of friction presented in Chapter 2, it is evident that the behavior of friction is significantly influenced by various factors, such as the specific system under investigation, the numerical modeling approach, and the physical conditions related to the environment and the probing of friction. In our study, we aim to investigate the frictional behavior of a Kirigami sheet under the effects of strain. Previous studies have demonstrated that strained Kirigami sheets are prone to exhibiting out-of-plane buckling [6, 7] which is indicative

of a possible transition between two distinct systems: an atomically flat interface and an asperity system. These systems are usually only studied separately, and thus our primary objective is to explore the potential frictional effects associated with system transitions resulting from the straining of a Kirigami sheet. In particular, we want to investigate the significance of the contact area and evaluate the hypothesis that reducing the contact area will lead to a decrease in friction. Additionally, we seek to examine the relationship between the friction-load curve and this phenomenon. For the sake of contributing new insight to the field of nanoscale friction, we are especially interested in non-linear dependencies between friction and stretching of various Kirigami designs. Drawing on this perspective, we aim to investigate the prospects of achieving a negative friction coefficient for a system of coupled load and stretch. The relevant understanding of how physical conditions affect frictional behavior in experimental and numerical studies will be considered in order to frame our results within the theoretical understanding.

To gain a more comprehensive understanding of the potential applications of Kirigami design, we aim to develop a dataset based on MD simulations that capture the frictional effects on Kirigami designs when subjected to stretching and loading. We intend to employ machine learning techniques to discern any meaningful trends in the data that may be used to inform future research endeavors. Specifically, we seek to leverage the machine learning model to facilitate an accelerated search for optimizing specific frictional properties. Our focus will be on evaluating the prospects of reducing or increasing the friction force, as well as reducing or increasing the friction coefficient for a coupled system of load and stretch. Our main research questions can be summarized as follows.

1. How can we design an MD simulation that provides a reliable foundation for an investigation of the friction behavior for a Kirigami graphene sheet sliding on a substrate? How do physical conditions such as temperature and sliding speed control the frictional behavior?
2. How can we design an ensemble of Kirigami patterns for the investigation of its frictional properties with the scope of getting out-of-plane buckling and also randomized design features?
3. Can we control friction for a Kirigami sheet through pattern design and stretching of the sheet?
 - (a) How does friction dependent on a changing contact area?
 - (b) How does the friction-load curve relate to stretched Kirigami sheets?
 - (c) Are the effects of stretching and pattern design significant when considered independently?
4. Is it possible to utilize machine learning techniques to identify general trends in friction associated with Kirigami designs, stretch and load?
5. Can we use a trained machine learning model to predict new designs through accelerated search?
6. What are the prospects of achieving a negative friction coefficient for a system of coupled load and stretch through Kirigami design?

Part II

Simulations

Chapter 3

Negative friction coefficient

For the final part of this thesis, we concern ourselves with a proof of concept approach for the designing of a negative friction coefficient. From the pilot study (??) we found the two investigated patterns to have a non-linear relationship with strain which is hypothesized to yield a negative friction coefficient in a coupled system system of load and strain for certain load ranges. We will investigate this hypothesis further in this chapter.

3.1 Nanomachine coupling

We do not attempt to simulate the dynamics of any nanomachine designs, but we propose that a coupling could be achieved, for instance by following a design as sketched in Fig. 3.1. Such a design could perhaps be achieved by rigging carbon nanotubes in a similar configuration.

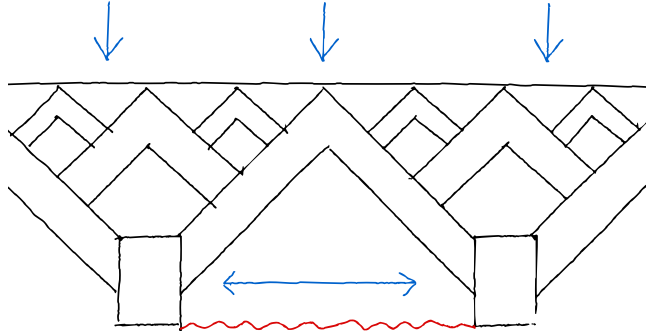


Figure 3.1: Working sketch for nanomachine

We mimic the nanomachine coupling by implementing a load-depending tension force to our MD simulations. So far, we have kept the pull block spaced by a fixed distance throughout the simulations, but now we let the pull blocks move relative to each other under the influence of this tension force between the blocks. The tension force F_t is modeled to be linearly coupled to normal load $F_t = TF_N$ by a factor T which represents the ratio for the load to strain coupling. We find that a ratio of $T = 6$ will provide the necessary tension for achieving a full strain range (till rupture) within the loading range used so far in our study. Notice that this coupling scheme is slightly different than that proposed in ?? where we assumed a coupling between load and strain $\varepsilon = RF_N$. This is done to provide a standardized description of the proposed nanomachine for which the relation between tension and strain will depend on the specific Kirigami sheet. We use the Tetrahedron (7, 5, 1) and Honeycomb (2, 2, 1, 5) from the pilot study and perform multiple simulations for different loads. We sample 100 pseudo uniform normal force values in the [0, 15] nN which corresponds to a tension force of [0, 90] nN. For the Tetrahedron pattern we increase the load by a speed of 0.015 nN/ps. Due to a rapid change in the strain-tension curve for the Honeycomb pattern we reduced the loading speed to 0.0015 nN/ps and added additional data points to the sparsely populated strain range. By considering the strain-load curve we map compare the results

from the pilot study ?? by mapping the strain values to the corresponding load values of our coupled system. The results are shown in Fig. 3.2.

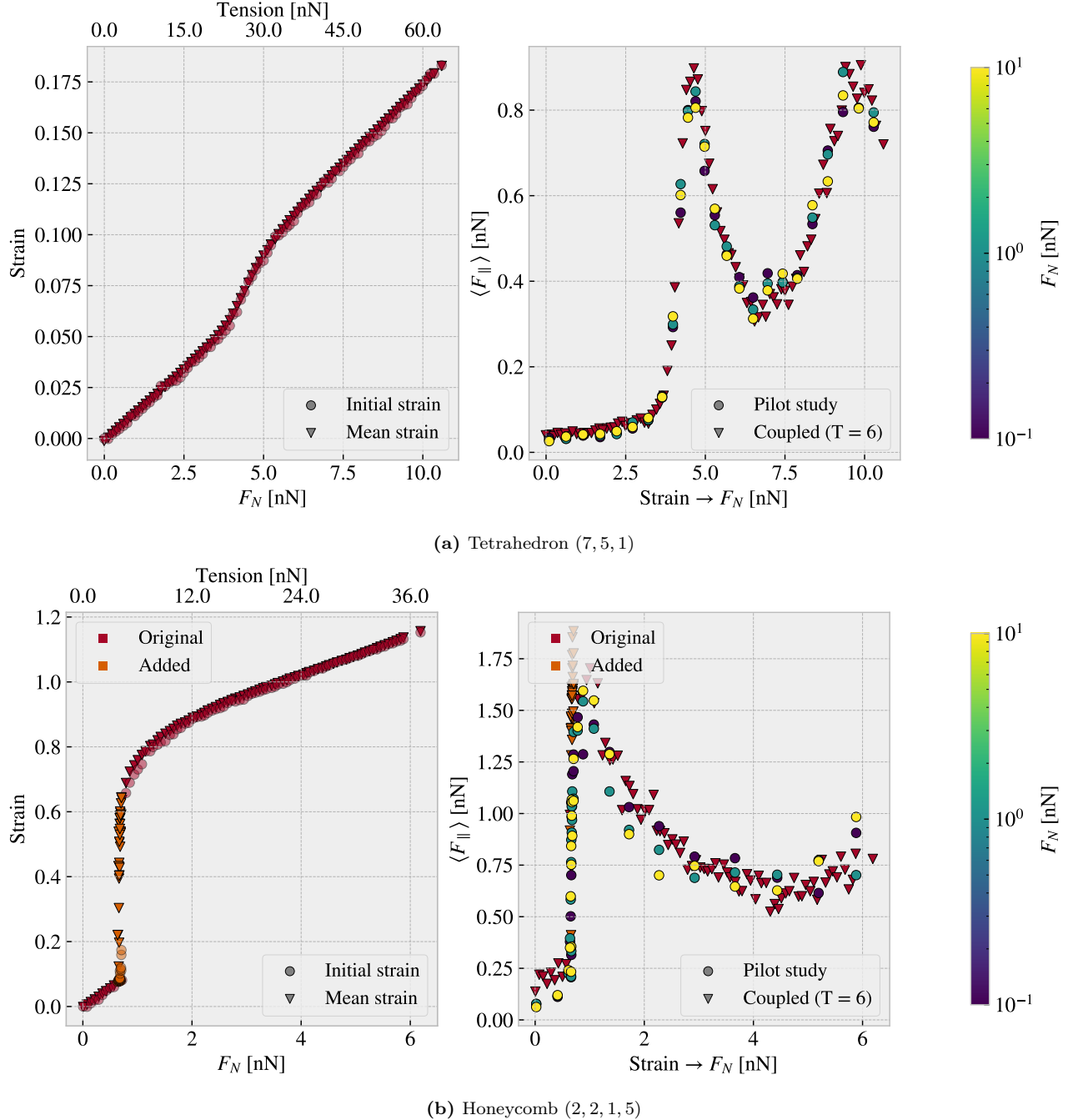


Figure 3.2: Evaluation of the friction response for a coupled system using (a) the Tetrahedron (7, 5, 1) and (b) Honeycomb (2, 2, 1, 5) pattern. The pull blocks are allowed to move relative to each other under the influence of a tension force F_t modeled as $F_t = RF_N$ for normal load F_N and a ratio $R = 6$. The right panel shows the friction vs. stretch curve in comparison to the locked pull block system and constantly defined normal from the pilot study (??). The left panel shows the strain-tension curve. For the Honeycomb pattern, we added more data points in the region where the strain-tension curve changed rapidly.

Generally, we observe from Fig. 3.2 that the data points of the coupled system aligns reasonable well with the mapped data points from the pilot study. This indicates that the simultaneous loading and straining of

the system does not suppress the underlying mechanism governing the non-linear trends. For the Tetrahedron pattern we find an almost linear strain-tension curve which makes for a recognizable trend in the friction-load curve similar to that seen in the friction-strain curve in ???. In both cases, we also notice that the initial and the mean strains aligns rather well. This suggest that the sliding does not contribute to a significantly increased tension in the sheet which would otherwise lead to an increased strain as well. For the Honeycomb pattern, we find an interesting trend for the strain-tension curve. At low tension, the curve of the strain is increasing seemingly linearly with strain, but a drastic increase in strain happens at a tension of 4.5 nN ($F_N = 0.75$ nN) transitioning from a strain of roughly 0.08 to 0.7. Eventually this settles off into a linear trend before reaching the rupture point. This reflects the reason for decreasing the loading speed and adding more data points to fill this gap in strain-tension curve. The rapid increase in the strain-load curve makes for a similar rapid increase in the friction-load curve as well. Hence we find that the Honeycomb coupled system essentially exhibit an intial discontinuous increase in friction with load, which is then followed by a longer region of decreasing friction with load. When considering the simulation frames in ?? we notice that the strain range covered in this transition aligns rather well with the unfolding of the honeycomb pattern. We have previously noted that the Honeycomb pattern unfolds in segments buckling one at a time. We observe that this unfolding is initiziated after passing a minimum tension. During the unfolding phase the friction increases, but immediately after friction decrease with further straining. Once again, this highlights that this transition might of interest for further investigations in order to get a better understanding of the underlying mechanisms being in play.

From the results in Fig. 3.2 we have found that our proposed coupled system, based on a $T = 6$ tension-load coupling, demonstrates a significant negative friction coefficient in certain load regions. By considering the maximum and minimum friction points along the friction-strain curve we find that this correponds to minimal friction coefficients μ_{\min} on the order of

$$\text{Tetrahedron: } \mu_{\min} \sim \frac{0.31 \text{ nN} - 0.90 \text{ nN}}{6.55 \text{ nN} - 4.65 \text{ nN}} = -0.31 \quad \text{Honeycomb: } \mu_{\min} \sim \frac{0.53 \text{ nN} - 1.88 \text{ nN}}{4.31 \text{ nN} - 0.71 \text{ nN}} = -0.38. \quad (3.1)$$

This result supports that the use of Kirigami sheet in a coupled system can be used to achieve a negative friction coefficients. In the pilot study (??) we estimated the Tetrahedron pattern to exhibit a coeffient following $-R12.75$ nN smaller than the Honeycomb following $-R2.72$ nN. From the results in Eq. (3.1) we find that the resulting coefficients a closer in value which we attribute to the difference in the strain-tension curve. However, we notice that both values can be scaled by increasing the strain-load coupling T , which would make for a more negative slope.

Chapter 4

Summary

In this thesis we have studied nanoscale friction of a Kirigami graphene sheet under the influence of load and strain using MD simulations. We have developed a numerical framework for generating various Kirigami designs which was used to create a dataset of the frictional behavior depending on the Kirigami pattern, strain and loading. Our findings suggest that the frictional behavior of a Kirigami sheet is highly dependent on the geometry of the pattern and the strain conditions. We observed that the out-of-plane buckling can be associated with a non-linear friction-strain curve which can be utilized to demonstrate a negative friction coefficient in a system with coupled load and strain. Moreover, we have investigated the possibility to use machine learning on this dataset and attempted an accelerated search. Our result suggest that machine learning can be feasible for this approach, but more data is needed to provide a more reliable foundation for a search of new Kirigami patterns. In this chapter we will summarize the findings in more detail and draw some conclusions. At the end we will provide some topics for further research.

4.1 Summary and conclusions

4.1.1 Designing an MD simulation

We have designed an MD simulation for the examination of friction for a graphene sheet sliding on a silicon substrate. The key system features were the introduction of the pull blocks, defined as the end regions of the sheet with respect to the sliding direction, which was utilized for applying normal load and sliding the sheet. The pull blocks were made partly rigid and used to employ a thermostat as well. By an analysis of the friction forces retrieved from sliding simulations we defined a standardized metric for kinetic friction. We measured the force acting from the substrate on the full sheet (including the pull blocks) with respect to the sliding direction and defined kinetic friction by the mean value of the last half of the simulation. The uncertainties were estimated on the basis of the fluctuations in the running mean. We found that the assessment of static friction was ambiguous for our simulation and did not pursue this further. From the analysis of the force traces, friction force vs. time, we identify the friction behavior in our simulation domain as being in the smooth sliding regime mainly due to the choice of sliding speed (20 m/s) and infinitely stiff springs. This was further supported by a demonstration of a transition to stick-slip behavior with softer springs and a lowering of sliding speed. By conducting a more systematic investigation of the effects of temperature, sliding speed, spring constant and timestep, we settled on the default values based on numerical stability and computational cost. We found that friction increased with temperature which we attribute to being in the ballistic sliding regime. We used the room temperature 300 K as a standard choice. Furthermore, we found friction to increase with velocity as expected, with some signs of phonon resonance at certain sliding speeds as well. We chose a rather high velocity of 20 m/s mainly for the consideration of computational costs. For the spring constant, we found decreasing friction with increasing stiffness of the springs which is associated with the transition from a stick-slip-influenced regime toward smooth sliding. The choice of an infinitely stiff spring was made from a stability assessment. Finally, we confirmed that a timestep of 1 fs provides reasonable numerical stability. However, based on fluctuations with timestep we find that the uncertainty in the simulations might be higher than first estimated.

4.1.2 Generetig Kirigami patterns

In order to invstigate the effects of Kirigami design we have created a numerical framework for generating various patterns. By defining an indexing system for the hexagonal lattice structure we were able to define the Kirigami designs as a 2D binary matrix for numerical implementation. We digitalized two different macroscale designs, which we named the *Tetrahedron* and *Honeycomb* pattern, that successfully produced out-of-plane buckling when stretched. Through our numerical framework we were able to create an ensemble of perturbed unique variations which yielded approximately 135k and 2025k for the Tetrahedron and Honeycomb patterns respectively. When considering the possibility to translate the patterns we find the ability to increase the number by roughly a factor 100. In addition we created a framework for generating random walk based Kirigami patterns. This was regulated by introducing features such as bias, avoidance of existing cuts, preference to keeping a direction and procedures to repairing the sheet for simulation purposes. In general, the capabilities of the numerical framework for generating Kirigami designs exceeded our computational resources with regard to performing MD simulation under different load and strain for each of the designs. Thus our MD-based dataset only utilized a subset of configurations with 9660 data points based on 216 Kirigami configurations (Tetrahedron: 68, Honeycomb: 45, Random walk: 100, Pilot study: 3). Thus our Kirigami generative framework can be valuable for further studies on an extended dataset.

4.1.3 Control friction using Kirigami

We have investigated the frictional behavior of the Tetrahedron and Honeycomb patterns in comparison to a non-cut sheet under various strains and loads. Initially, we observed that straining the Kirigami sheets in vacuum resulted in an out-of-plane buckling. When adding the substrate to the simulation this translated into a decreasing contact area with strain. We found the Honeycomb sheet to exhibit the most significant buckling with a corresponding reduction of relative contact area to approximately 43%. The non-cut sheet did not produce any significant buckling in comparison. We found that friction generally increased with strain which contradicts the asperity theory hypothesis of decreasing friction with decreasing contact area. Moreover, the friction-strain curve exhibited highly non-linear trends with strong negative slopes (see ??), while the non-cut sheet did not show any significant dependency on the strain. We also found that the non-stretched Kirigami patterns did affect friction to some degree, but this was one order of magnitude lower than the effects associated with the strain in combination. This led us to the conclusion that the changing contact area cannot be regarded as a dominant mechanism for friction in the Kirigami sheet system nor the independent consideration of sheet configuration or tension in the sheet. When considering the dependency with load we generally found a weak dependency which can be associated with a friction coefficient on the order of 10^{-4} – 10^{-5} even though we could not confirm any clear relationship. This is best attributed to a superlubric state of the graphene sheet as seen in other studies as well. The slope of the friction-load curves was not considerably affected by the straining of the Kirigami sheet which led us to the conclusion that the strain-induced effects are dominant in comparison to any load-related effects. By proposing a linear coupling between load and strain with ratio R we find that these results suggest the possibility to find negative friction coefficients in certain load ranges following $-R12.75\text{ nN}$ for the Tetrahedon and $-R \cdot 2.72\text{ nN}$ for the Honeycomb pattern.

4.1.4 Capture trends with machine learning

The dataset reveals some general correlations with mean friction, such as a positive correlation to strain (0.77) and porosity (0.60), and a negative correlation to contact area (-0.67). These results align with the finding in the pilot study, suggesting that the change in friction is associated with cuts in the sheet (porosity) and a changing contact area.

By defining the friction property metrics: $\min F_{\text{fric}}$, $\max F_{\text{fric}}$, $\max \Delta F_{\text{fric}}$ and $\max \text{drop}$ (maximum decrease in friction with strain), we investigated the top candidates within our dataset. From these results, we found no incentive for the possibility to reduce friction with the Kirigami approach since the non-cut sheet provided the lowest overall friction. Regarding the maximum properties, we found an improvement from the original pilot study values and with the Honeycomb pattern producing the highest scores. This suggests that the data contains some relevant information for optimization with respect to these properties. Among the top candidates, we found that a flat friction-strain profile is mainly associated with little decrease in the contact area and vice versa which again aligns with the pilot study findings.

For the machine learning investigation, we have implemented a VGGNet-16-inspired convolutional neural network with a deep “stairlike” architecture: C32-C64-C128-C256-C512-C1024-D1024-D512-D256-D128-D64-D32, for convolutional layers C with the number denoting channels and fully connected (dense) layers D with the number denoting nodes. The final model contains 1.3×10^7 parameters and was trained using the ADAM optimizer for a cyclic learning rate and momentum scheme. We trained the network for a 1000 epochs while saving the best model during training based on the validation score. The model validation performance gives a mean friction R^2 score of $\sim 98\%$ and a rupture accuracy of $\sim 96\%$. However, we got lower scores for a selected subset of the Tetrahedon ($R^2 \sim 88.7\%$) and Honeycomb ($R^2 \sim 96.6\%$) pattern based on the top 10 max drop scores respectively. These scores were lower despite the fact that the selected set was partly included in the training data as well in addition to the fact that the hyperparameter selection favored the performance on this selected set as well. Thus we conclude that these selected configurations, associated with a highly non-linear friction-strain curve, represent a bigger challenge for the machine learning prediction. One interpretation is that these involve the most complex dynamics and perhaps that this is not readily distinguished from the behavior of the other configurations which constitute the majority of the data set. By evaluating the ability of the model to rank the dataset according to the property scores we found in general a good representation of the top 3 scores for the maximum categories, while the minimum friction property ranking was lacking. We attribute this latter observation to a higher need for precision which the model did not possess.

In order to provide a more true evaluation of the model performance we created a test set based on MD simulations for an extended Random walk search. This test revealed a significantly worse performance than seen for the validation set with a two-order of magnitude higher loss and a negative friction mean R^2 score which corresponds to the prediction being worse than simply guessing on the true data mean. However, by reconsidering the choice of architecture complexity hypertuning with respect to the validation loss, we found similar poor results on the test set. This indicates, that the test score is not simply a product of a biased hypertuning process but instead points to the fact that our original dataset did not cover a wide enough configuration distribution to accurately capture the full physical complexity of the Kirigami friction behavior. Based on the validation scores we conclude that the use of machine learning is feasible, but that we need to improve the dataset in order to reach a reliable model.

4.1.5 Accelerated search

Using the ML model we performed two types of accelerated search. One by evaluating the property scores of an extended dataset and another with the use of the genetic algorithm approach. For the extended dataset search, we used the developed pattern generators to generate $135\text{ k} \times 10$ Tetrahedon, $2025\text{ k} \times 10$ Honeycomb and 10 k Random walk patterns. For the minimum friction property, the search suggests a favoring of a low cut density (low porosity) which aligns with the overall idea that the dataset does not provide an incentive for further friction reduction with the non-cut sheet resulting in the lowest friction. The maximum properties resulted in some minor score increases but the suggested candidates were mainly overlapping with the original dataset. By investigating the model prediction sensitivity to the translation of the Tetrahedron and Honeycomb patterns we found that the model predictions varied drastically with small translations. This can be attributed to a physical dependency since the edge of the sheet is affected by this translation. However, due to the poor model performance on the test set, we find it more likely to be a model insufficiency related to the lacking dataset.

For the genetic algorithm approach, we investigated the optimization for the max drop property using starting population based on the result from the extended dataset accelerated search, and some random noise initializations with different porosity values. This approach did not provide any noteworthy incentive for new design structures worth more investigation. In general, the initialization of the population itself proved to be a more promising strategy than the genetic algroithm. However, this is highly affected by the uncertainty of the model predictions, and thus we did not pursue this any further. By considering the Grad-CAM explanation method we found that the model predictions occasionally payed considerable attention to the top and bottom edge of the configurations. This is surprising since these are not true edges but are connected to the pull blocks in the simulation. Despite the uncertainties in the predictions, we argue that this might be attributed to thermostat effects from the pull blocks and thus we note this as a feature worth investigating in the simulations.

4.1.6 Negative friction coefficient

By enforcing a coupling between load and sheet tension, mimicking a nanomachine attached to the sheet, we investigated the load curves arising from the loading of the Tetrahedron (7, 5, 1) and Honeycomb (2, 2, 1, 5) pattern from the pilot study. The non-linear trend observed for increasing strain carried over to the coupled system as well producing a highly non-linear friction-load curve. The Honeycomb pattern exhibited additionally a non-linear strain-tension curve which resulted in an almost discontinuous increase in friction for the initial increase in load. We attribute this feature to an unfolding process visually confirmed from the simulation frames. For the coupled system with a load-to-tension ratio of 6 we found regions in the friction-load curve with significant negative slopes. By considering the maximum and minimum points for such regions we estimated the average friction coefficient to be -0.31 in the range $F_N = [4.65, 6.55]$ nN for the Tetrahedron pattern and -0.38 in the range $F_N = [0.71, 4.31]$ nN for the Honeycomb pattern.

Our findings suggest that the combined use of Kirigami cuts and strain has considerable potential for friction control, especially under the influence of a coupled system of load and strain.

4.2 Outlook

In this thesis, we have successfully shown that certain Kirigami designs exhibit non-linear behavior with strain. This discovery was done through a focus on the exploration of the effects of different designs. This invites further investigation of the underlying mechanisms behind this phenomenon. By considering one or two design, based on Tetrahedron and Honeycomb patterns, it would be valuable to investigate the effects on the friction-strain curve under various physical parameters.

First of all, we suggest an investigation of how the friction-strain curve depends on temperature, sliding speed, spring constant, and loads for an increased range $F_N > 100nN$. This is especially interesting in the context of physical conditions leading to a stick-slip behavior since our study takes a basis in smooth sliding friction. Moreover, it would be valuable to verify that the choices for relaxation time, pauses, interatomic potentials and substrate material are not critical for the qualitative observations. Especially the Adaptive Intermolecular Reactive Empirical Bond Order (AIREBO) potential for the modeling of the graphene sheet might be of interest. In this context, it might also be useful to investigate the effects of excluding adhesion in the simulations. In order to gain further insight into the role of commensurability one could vary the scan angle as well. Since we suspect that our simulation corresponds to a incommensurable superlubric state, certain scan angles are hypothesized to yield higher friction. If the friction-strain curve is based on a commensurability effect this might yield qualitative different results and perhaps also allowing for a lowering of friction with strain. We might also consider investigating the friction-strain relationship under a uniform load to get insight into how the loading distribution effects the out-of-plane buckling and associated frictional effects.

Another topic worth studying is the relation to scale and edge effects. This includes an investigation of scaling effects, considering the ratio of the sheet to the edge, but also a translation of the sheet patterns to study the presence of any Kirigami-induced edge effects. The latter is motivated by the findings from the machine learning predictions. With this regard, we would also suggest a more detailed study of the effect of the thermostat in the pull blocks which is suggested to have a possibly importance when judging from the Grad-CAM analysis.

For the machine learning approach, our findings suggest that the dataset is extended considerably. This can be done with respect to the aim of exploring Kirigami configurations as done in this thesis, but it can also be done for a single configuration under variation of some of the simulation parameters to support some of the above mentioned investigations. In that context, one could consider more advanced model architectures and machine learning techniques. If successful this would invite further studies of inverse design methods such as GAN or diffusion models.

Appendices

Appendix A

Appendix A

Appendix A

Appendix B

Appendix B

Appendix C

Bibliography

- ¹E. Gnecco and E. Meyer, *Elements of friction theory and nanotribology* (Cambridge University Press, 2015).
- ²Bhusnur, “Introduction”, in *Introduction to tribology* (John Wiley & Sons, Ltd, 2013) Chap. 1, 1–?
- ³H.-J. Kim and D.-E. Kim, “Nano-scale friction: a review”, *International Journal of Precision Engineering and Manufacturing* **10**, 141–151 (2009).
- ⁴K. Holmberg and A. Erdemir, “Influence of tribology on global energy consumption, costs and emissions”, *Friction* **5**, 263–284 (2017).
- ⁵B. Bhushan, “Gecko feet: natural hairy attachment systems for smart adhesion – mechanism, modeling and development of bio-inspired materials”, in *Nanotribology and nanomechanics: an introduction* (Springer Berlin Heidelberg, Berlin, Heidelberg, 2008), pp. 1073–1134.
- ⁶P. Z. Hanakata, E. D. Cubuk, D. K. Campbell, and H. S. Park, “Accelerated search and design of stretchable graphene kirigami using machine learning”, *Phys. Rev. Lett.* **121**, 255304 (2018).
- ⁷P. Z. Hanakata, E. D. Cubuk, D. K. Campbell, and H. S. Park, “Forward and inverse design of kirigami via supervised autoencoder”, *Phys. Rev. Res.* **2**, 042006 (2020).
- ⁸L.-K. Wan, Y.-X. Xue, J.-W. Jiang, and H. S. Park, “Machine learning accelerated search of the strongest graphene/h-bn interface with designed fracture properties”, *Journal of Applied Physics* **133**, 024302 (2023).
- ⁹Y. Mao, Q. He, and X. Zhao, “Designing complex architected materials with generative adversarial networks”, *Science Advances* **6**, eaaz4169 (2020).
- ¹⁰Z. Yang, C.-H. Yu, and M. J. Buehler, “Deep learning model to predict complex stress and strain fields in hierarchical composites”, *Science Advances* **7**, eabd7416 (2021).
- ¹¹A. E. Forte, P. Z. Hanakata, L. Jin, E. Zari, A. Zareei, M. C. Fernandes, L. Sumner, J. Alvarez, and K. Bertoldi, “Inverse design of inflatable soft membranes through machine learning”, *Advanced Functional Materials* **32**, 2111610 (2022).
- ¹²S. Chen, J. Chen, X. Zhang, Z.-Y. Li, and J. Li, “Kirigami/origami: unfolding the new regime of advanced 3D microfabrication/nanofabrication with “folding””, *Light: Science & Applications* **9**, 75 (2020).
- ¹³Z. Deng, A. Smolyanitsky, Q. Li, X.-Q. Feng, and R. J. Cannara, “Adhesion-dependent negative friction coefficient on chemically modified graphite at the nanoscale”, *Nature Materials* **11**, 1032–1037 (2012).
- ¹⁴B. Liu, J. Wang, S. Zhao, C. Qu, Y. Liu, L. Ma, Z. Zhang, K. Liu, Q. Zheng, and M. Ma, “Negative friction coefficient in microscale graphite/mica layered heterojunctions”, *Science Advances* **6**, eaaz6787 (2020).
- ¹⁵D. Mandelli, W. Ouyang, O. Hod, and M. Urbakh, “Negative friction coefficients in superlubric graphite–hexagonal boron nitride heterojunctions”, *Phys. Rev. Lett.* **122**, 076102 (2019).
- ¹⁶R. W. Liefferink, B. Weber, C. Coulais, and D. Bonn, “Geometric control of sliding friction”, *Extreme Mechanics Letters* **49**, 101475 (2021).
- ¹⁷N Manini, O. M. Braun, E Tosatti, R Guerra, and A Vanossi, “Friction and nonlinear dynamics”, *Journal of Physics: Condensed Matter* **28**, 293001 (2016).
- ¹⁸B. Bhushan and A. V. Kulkarni, “Effect of normal load on microscale friction measurements”, *Thin Solid Films* **278**, 49–56 (1996).
- ¹⁹B. P. Hung, P. Y. Huri, J. P. Temple, A. Dorafshar, and W. L. Grayson, “Chapter 10 - craniomaxillofacial bone”, in *3d bioprinting and nanotechnology in tissue engineering and regenerative medicine*, edited by L. G. Zhang, J. P. Fisher, and K. W. Leong (Academic Press, 2015), pp. 215–230.

- ²⁰J. Gao, W. D. Luedtke, D. Gourdon, M. Ruths, J. N. Israelachvili, and U. Landman, “Frictional forces and amontons’ law: from the molecular to the macroscopic scale”, *The Journal of Physical Chemistry B* **108**, Publisher: American Chemical Society, 3410–3425 (2004).
- ²¹J. H. Dieterich, “Time-dependent friction in rocks”, *Journal of Geophysical Research (1896-1977)* **77**, 3690–3697 (1972).
- ²²R. Burridge and L. Knopoff, “Model and theoretical seismicity”, *Bulletin of the Seismological Society of America* **57**, 341–371 (1967).
- ²³O. M. Braun and J. Röder, “Transition from stick-slip to smooth sliding: an earthquakelike model”, *Phys. Rev. Lett.* **88**, 096102 (2002).
- ²⁴W. I. Newman and A. M. Gabrielov, “Failure of hierarchical distributions of fibre bundles. I”, *International Journal of Fracture* **50**, 1–14 (1991).
- ²⁵R. F. Smalley Jr., D. L. Turcotte, and S. A. Solla, “A renormalization group approach to the stick-slip behavior of faults”, *Journal of Geophysical Research: Solid Earth* **90**, 1894–1900 (1985).
- ²⁶P. Selvadurai, P. Galvez, P. Mai, and S. Glaser, “Modeling frictional precursory phenomena using a wear-based rate- and state-dependent friction model in the laboratory”, *Tectonophysics* **847**, 229689 (2023).
- ²⁷Y. Mo, K. T. Turner, and I. Szlufarska, “Friction laws at the nanoscale”, *Nature* **457**, 1116–1119 (2009).
- ²⁸G. Carbone and F. Bottiglione, “Asperity contact theories: do they predict linearity between contact area and load?”, *Journal of the Mechanics and Physics of Solids* **56**, 2555–2572 (2008).
- ²⁹F. Bowden and D. Tabor, *The friction and lubrication of solids*, International series of monographs on physics vb. 1 (Clarendon Press, 2001).
- ³⁰H.-J. Kim and D.-E. Kim, “Molecular dynamics simulation of atomic-scale frictional behavior of corrugated nano-structured surfaces”, *Nanoscale* **4**, 3937–3944 (2012).
- ³¹W. Commons, *File:asperities.svg — wikimedia commons, the free media repository*, [Online; accessed 3-February-2023], 2022.
- ³²I. Szlufarska, M. Chandross, and R. W. Carpick, “Recent advances in single-asperity nanotribology”, *Journal of Physics D: Applied Physics* **41**, 123001 (2008).
- ³³G. Binnig, C. F. Quate, and C. Gerber, “Atomic force microscope”, *Phys. Rev. Lett.* **56**, 930–933 (1986).
- ³⁴S. S. Perry, “Scanning Probe Microscopy Measurements of Friction”, *MRS Bulletin* **29**, 478–483 (2004).
- ³⁵Hertz, “On the contact of elastic solids”, *Crelle’s Journal* **92**, 156–171.
- ³⁶D. Maugis, “Adhesion of spheres: the jkr-dmt transition using a dugdale model”, *Journal of Colloid and Interface Science* **150**, 243–269 (1992).
- ³⁷M. H. Müser, “Rigorous field-theoretical approach to the contact mechanics of rough elastic solids”, *Phys. Rev. Lett.* **100**, 055504 (2008).
- ³⁸B. N. J. Persson, “Theory of rubber friction and contact mechanics”, *The Journal of Chemical Physics* **115**, 3840–3861 (2001).
- ³⁹J. A. Greenwood and J. B. P. Williamson, *Contact of nominally flat surfaces*, en, 1966.
- ⁴⁰A. Bush, R. Gibson, and T. Thomas, “The elastic contact of a rough surface”, *Wear* **35**, 87–111 (1975).
- ⁴¹B. Luan and M. O. Robbins, “The breakdown of continuum models for mechanical contacts”, *Nature* **435**, 929–932 (2005).
- ⁴²Y. Dong, A. Vadakkepatt, and A. Martini, “Analytical models for atomic friction”, *Tribology Letters* **44**, 10.1007/s11249-011-9850-2 (2011).
- ⁴³E. Gnecco, R. Bennewitz, T. Gyalog, C. Loppacher, M. Bammerlin, E. Meyer, and H.-J. Güntherodt, “Velocity dependence of atomic friction”, *Phys. Rev. Lett.* **84**, 1172–1175 (2000).
- ⁴⁴P. Hänggi, P. Talkner, and M. Borkovec, “Reaction-rate theory: fifty years after kramers”, *Rev. Mod. Phys.* **62**, 251–341 (1990).
- ⁴⁵Y. Sang, M. Dubé, and M. Grant, “Thermal effects on atomic friction”, *Phys. Rev. Lett.* **87**, 174301 (2001).

- ⁴⁶S. Y. Krylov, K. B. Jinesh, H. Valk, M. Dienwiebel, and J. W. M. Frenken, “Thermally induced suppression of friction at the atomic scale”, *Phys. Rev. E* **71**, 065101 (2005).
- ⁴⁷S. Krylov and J. Frenken, “Thermal contact delocalization in atomic scale friction: a multitude of friction regimes”, English, *New Journal of Physics* **9**, 10.1088/1367-2630/9/10/398 (2007).
- ⁴⁸K. B. Jinesh, S. Y. Krylov, H. Valk, M. Dienwiebel, and J. W. M. Frenken, “Thermolubricity in atomic-scale friction”, *Phys. Rev. B* **78**, 155440 (2008).
- ⁴⁹M. H. Müser, “Nature of mechanical instabilities and their effect on kinetic friction”, *Phys. Rev. Lett.* **89**, 224301 (2002).
- ⁵⁰Q. Li, Y. Dong, D. Perez, A. Martini, and R. W. Carpick, “Speed dependence of atomic stick-slip friction in optimally matched experiments and molecular dynamics simulations”, *Phys. Rev. Lett.* **106**, 126101 (2011).
- ⁵¹Y. Dong, Q. Li, and A. Martini, “Molecular dynamics simulation of atomic friction: a review and guide”, *Journal of Vacuum Science & Technology A* **31**, 030801 (2013).
- ⁵²K. Johnson and J. Woodhouse, “Stick-slip motion in the atomic force microscope”, *Tribology Letters* **5**, 155–160 (1998).
- ⁵³S. N. Medyanik, W. K. Liu, I.-H. Sung, and R. W. Carpick, “Predictions and observations of multiple slip modes in atomic-scale friction”, *Phys. Rev. Lett.* **97**, 136106 (2006).
- ⁵⁴A. Vanossi, N. Manini, M. Urbakh, S. Zapperi, and E. Tosatti, “Modeling friction: from nanoscale to mesoscale”, *Reviews of Modern Physics* **85**, 529–552 (2013).
- ⁵⁵J. Frenkel and T. Kontorova, “On the theory of plastic deformation and twinning”, *Phys. Z. Soviet.* **13** (1938).
- ⁵⁶J. Norell, A. Fasolino, and A. Wijn, “Emergent friction in two-dimensional frenkel-kontorova models”, *Physical Review E* **94**, 10.1103/PhysRevE.94.023001 (2016).
- ⁵⁷M. Dienwiebel, N. Pradeep, G. S. Verhoeven, H. W. Zandbergen, and J. W. Frenken, “Model experiments of superlubricity of graphite”, *Surface Science* **576**, 197–211 (2005).
- ⁵⁸C. Kittel, *Introduction to solid state physics*, 8th ed. (Wiley, 2004).
- ⁵⁹J. A. van den Ende, A. S. de Wijn, and A. Fasolino, “The effect of temperature and velocity on superlubricity”, *Journal of Physics: Condensed Matter* **24**, 445009 (2012).
- ⁶⁰M. Weiss and F.-J. Elmer, “Dry friction in the Frenkel-Kontorova-Tomlinson model: dynamical properties”, *Zeitschrift für Physik B Condensed Matter* **104**, 55–69 (1997).
- ⁶¹B. Bhushan, “Nanotribology and nanomechanics”, *Wear* **259**, 15th International Conference on Wear of Materials, 1–? (2005).
- ⁶²O. Penkov, H.-J. Kim, H.-J. Kim, and D.-E. Kim, “Tribology of graphene: A review”, *International Journal of Precision Engineering and Manufacturing* **15**, 577–585 (2014).
- ⁶³X. Zhao, M. Hamilton, W. G. Sawyer, and S. S. Perry, “Thermally activated friction”, *Tribology Letters* **27**, 113–117 (2007).
- ⁶⁴G Paolicelli, M Tripathi, V Corradini, A Candini, and S Valeri, “Nanoscale frictional behavior of graphene on sio₂ and ni(111) substrates”, *Nanotechnology* **26**, 055703 (2015).
- ⁶⁵S. Zhang, Y. Hou, S. Li, L. Liu, Z. Zhang, X.-Q. Feng, and Q. Li, “Tuning friction to a superlubric state via in-plane straining”, *Proceedings of the National Academy of Sciences* **116**, Publisher: Proceedings of the National Academy of Sciences, 24452–24456 (2019).
- ⁶⁶M. R. Vazirisereshk, H. Ye, Z. Ye, A. Otero-de-la Roza, M.-Q. Zhao, Z. Gao, A. T. C. Johnson, E. R. Johnson, R. W. Carpick, and A. Martini, “Origin of nanoscale friction contrast between supported graphene, mos₂, and a graphene/mos₂ heterostructure”, *Nano Letters* **19**, PMID: 31267757, 5496–5505 (2019).
- ⁶⁷H. M. Yoon, Y. Jung, S. C. Jun, S. Kondaraju, and J. S. Lee, “Molecular dynamics simulations of nanoscale and sub-nanoscale friction behavior between graphene and a silicon tip: analysis of tip apex motion.”, *Nanoscale* **7** **14**, 6295–303 (2015).
- ⁶⁸S. Li, Q. Li, R. W. Carpick, P. Gumbsch, X. Z. Liu, X. Ding, J. Sun, and J. Li, “The evolving quality of frictional contact with graphene”, *Nature* **539**, Number: 7630, 541–545 (2016).

- ⁶⁹A. Wijn, A. Fasolino, A. Filippov, and M. Urbakh, “Low friction and rotational dynamics of crystalline flakes in solid lubrication”, *Europhysics Letters (epl)* **95**, 10.1209/0295-5075/95/66002 (2011).
- ⁷⁰X. Feng, S. Kwon, J. Y. Park, and M. Salmeron, “Superlubric sliding of graphene nanoflakes on graphene”, *ACS Nano* **7**, Publisher: American Chemical Society, 1718–1724 (2013).
- ⁷¹F. Bonelli, N. Manini, E. Cadelano, and L. Colombo, “Atomistic simulations of the sliding friction of graphene flakes”, *The European Physical Journal B* **70**, 449–459 (2009).
- ⁷²M. Reguzzoni, A. Fasolino, E. Molinari, and M. C. Righi, “Friction by shear deformations in multilayer graphene”, *The Journal of Physical Chemistry C* **116**, 21104–21108 (2012).
- ⁷³Y. Liu, F. Grey, and Q. Zheng, “The high-speed sliding friction of graphene and novel routes to persistent superlubricity”, *Scientific Reports* **4**, 4875 (2014).
- ⁷⁴P. Zhu and R. Li, “Study of nanoscale friction behaviors of graphene on gold substrates using molecular dynamics”, *Nanoscale Research Letters* **13**, 34 (2018).
- ⁷⁵J. Zhang, E. Osloub, F. Siddiqui, W. Zhang, T. Ragab, and C. Basaran, “Anisotropy of graphene nanoflake–diamond interface frictional properties”, *Materials* **12**, 10.3390/ma12091425 (2019).
- ⁷⁶A. Sircar and P. K. Patra, “A simple generalization of Prandtl–Tomlinson model to study nanoscale rolling friction”, *Journal of Applied Physics* **127**, 135102, 10.1063/1.5143062 (2020).
- ⁷⁷M. Reguzzoni and M. C. Righi, “Size dependence of static friction between solid clusters and substrates”, *Phys. Rev. B* **85**, 201412 (2012).
- ⁷⁸N. Varini, A. Vanossi, R. Guerra, D. Mandelli, R. Capozza, and E. Tosatti, “Static friction scaling of physisorbed islands: the key is in the edge”, *Nanoscale* **7**, 2093–2101 (2015).
- ⁷⁹T. Fileteer, J. L. McChesney, A. Bostwick, E. Rotenberg, K. V. Emtsev, T. Seyller, K. Horn, and R. Bennewitz, “Friction and dissipation in epitaxial graphene films”, *Phys. Rev. Lett.* **102**, 086102 (2009).
- ⁸⁰C. Lee, Q. Li, W. Kalb, X. Liu, H. Berger, R. Carpick, and J. Hone, “Frictional characteristics of atomically thin sheets”, *Science (New York, N.Y.)* **328**, 76–80 (2010).
- ⁸¹E. Thormann, “Negative friction coefficients”, *Nature Materials* **12**, 468–468 (2013).
- ⁸²O Zwörner, H Hölscher, U. Schwarz, and R Wiesendanger, “The velocity dependence of frictional forces in point-contact friction”, *APPLIED PHYSICS A MATERIALS SCIENCE AND PROCESSING* **66**, S263–S268 (1998).
- ⁸³R. Guerra, U. Tartaglino, A. Vanossi, and E. Tosatti, “Ballistic nanofriction”, *Nature Materials* **9**, 634–637 (2010).